How Magnetic Particle Imaging Works

2

Contents

2.1 Introduction

In this chapter, the basic concepts of MPI are introduced. In order to get MPI to work, two basic ingredients are needed: First, one has to find a way to get the particles to emit some kind of characteristic signal that reveals their existence. To end up at a quantitative method, this signal should also carry information about the amount of magnetic material, i.e., the *particle concentration*. How this *signal encoding* is done in MPI is explained in Sect. 2.3. As a second component, one needs a way to determine where the signal comes from in relation to the object under examination. This usually is called *spatial encoding* and is achieved by making the emitted characteristic particle signal spatially dependent. In Sect. 2.4, the basic principle of spatial encoding is introduced. As it turns out, the simplest method for spatial encoding is rather slow and cannot fulfill the real-time requirements that potential applications have. Therefore, the subject of Sect. 2.5 is a way to improve the MPI performance with respect to acquisition time. Still, this performance upgrade is only capable of imaging small volumes of few centimeters in length. To circumvent this size limitation, in Sect. 2.6 a way to handle large imaging volumes is introduced. Finally in Sect. 2.7, limitations of MPI in spatial resolution and sensitivity are discussed.

T. Knopp, T.M. Buzug, *Magnetic Particle Imaging*,
DOI 10.1007/978-3-642-04199-0_2, © Springer-Verlag Berlin Heidelberg 2012

2.2 Magnetic Particles

The aim of the MPI method is to determine the spatial distribution of magnetic material, injected into the human body. One suitable magnetic material for MPI is iron oxide, which usually is available in the form of iron oxide–based nanoparticles. Such particles consist of a core, which is responsible for its magnetic behavior, and a magnetically neutral coating, which prevents agglomeration of the particles. In Fig. 2.1, a schematic drawing of a spherical magnetic nanoparticle is shown. Typically, the diameter of the particle core is in the range of 1–100 nm. In Fig. 2.2, a picture of magnetic nanoparticles developed at the University of Lübeck is shown (see [LBBS$^+$09a]). One way to visualize the shape of the particle core is transmission electron microscopy (TEM). In Fig. 2.3, a TEM picture of a fraction of the commercial tracer Resovist® (Bayer Schering Pharma) is shown (see [LBM08]).

If the particle coating is sufficiently thick, the nanoparticles show a *superparamagnetic* behavior. This means that the particle–particle interactions are negligibly small such that each particle has its own magnetic domain – the particles are said to be single domain. The prefix "super" essentially means that each particle behaves like a paramagnet with a large magnetic moment, which is significantly higher than the atomic moment [BL59].

2.2.1 Particle Concentration

Due to the small particle size in the nanometer range, it is not possible to determine the precise position of a particular particle using the MPI method. Instead, one images a map of the spatial particle concentration, which is usually displayed as

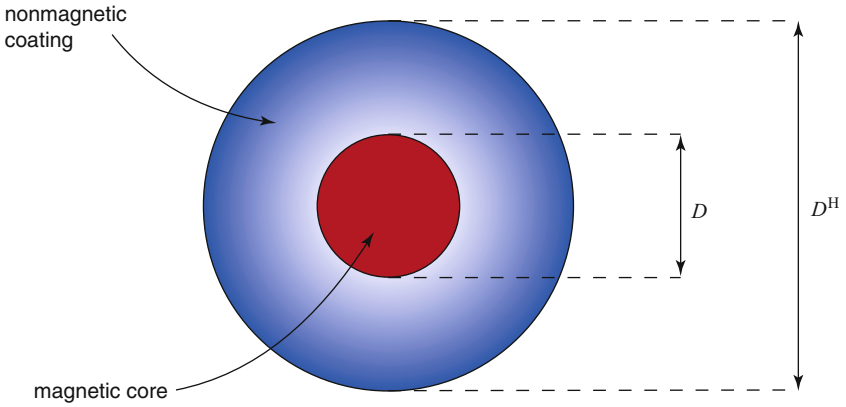

Fig. 2.1 Schematic drawing of a spherical magnetic nanoparticle consisting of a magnetic core (usually magnetite) and a magnetically neutral coating necessary to prevent agglomeration

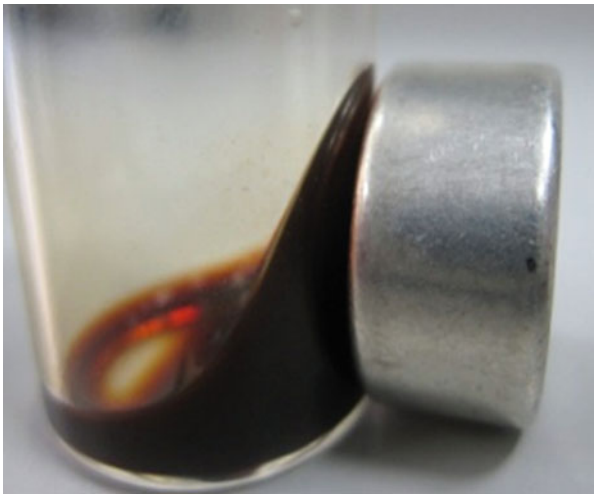

Fig. 2.2 Magnetic nanoparticles developed at the University of Lübeck in fluidal form. Using a permanent magnet (shown on the *right*) the particles can be magnetized (Courtesy of Kerstin Lüdtke-Buzug, University of Lübeck)

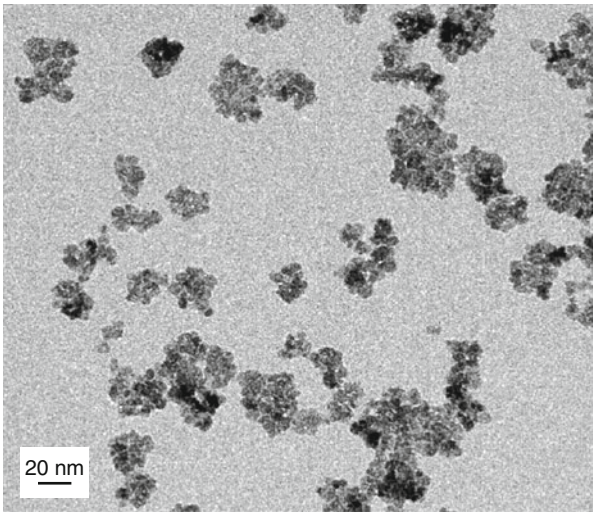

Fig. 2.3 TEM picture of a fraction of Resovist® particles visualizing the particles' iron-oxide core (Courtesy of Gunnar Schütz, Bayer Pharma AG)

a gray-value image, where white indicates a high particle concentration and black indicates vanishing particle concentration (see Fig. 2.4). The particle concentration is defined as the number of particles per volume, i.e.,

$$c := \frac{N^{\mathrm{P}}}{\Delta V}. \tag{2.1}$$

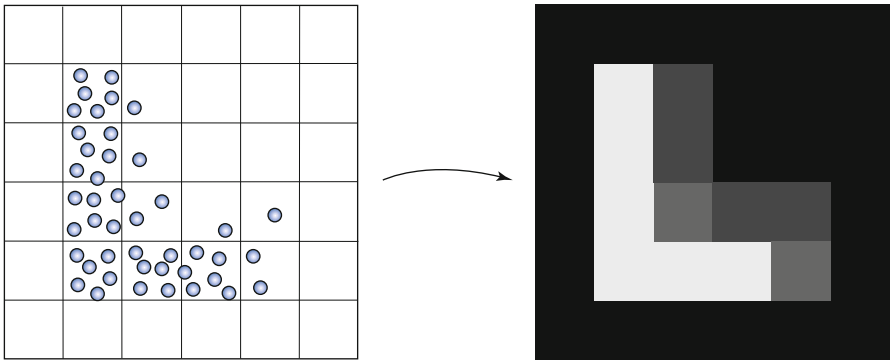

Fig. 2.4 Distribution of magnetic nanoparticles and a gray-value image of the discretized particle concentration

Here, N^{P} denotes the number of particles in a small volume ΔV, which has the role of an image voxel. The particle concentration depends on the spatial position, which is denoted by $\boldsymbol{r} = (x, y, z)^{\mathsf{T}}$ in this book.

2.2.2 Particle Magnetization

A basic theory for describing the magnetic behavior of superparamagnetic particles is the Langevin theory, which is defined under the assumption that the particles are always in thermal equilibrium. The magnetic behavior of each particle is described by its *magnetic moment* $\boldsymbol{m}$. Due to Brownian motion, the directions of the particles' magnetic moments are randomly distributed (see Fig. 2.5). Therefore, on a macroscopic scale, the sum of the magnetic moments is zero. The density of the sum of all magnetic moments is called *magnetization:*

$$\boldsymbol{M} := \frac{1}{\Delta V} \sum_{j=0}^{N^{\mathrm{P}}-1} \boldsymbol{m}_j \,. \tag{2.2}$$

When applying an external magnetic field, the particles start to align with the applied field such that a magnetization in direction of the applied field can be observed. Ignoring relaxation effects, the magnetization can be thus written as

$$\boldsymbol{M}(\boldsymbol{H}) = M(H)\boldsymbol{e}_{\boldsymbol{H}} \,, \tag{2.3}$$

where $M := \|\boldsymbol{M}\|_2$ denotes the length of the magnetization vector, $H := \|\boldsymbol{H}\|_2$ denotes the length of the magnetic field vector, and

$$\boldsymbol{e}_{\boldsymbol{H}} := \begin{cases} \dfrac{\boldsymbol{H}}{H} & H > 0 \\ \boldsymbol{0} & H = 0 \end{cases} \tag{2.4}$$

denotes the direction of the magnetic field strength.

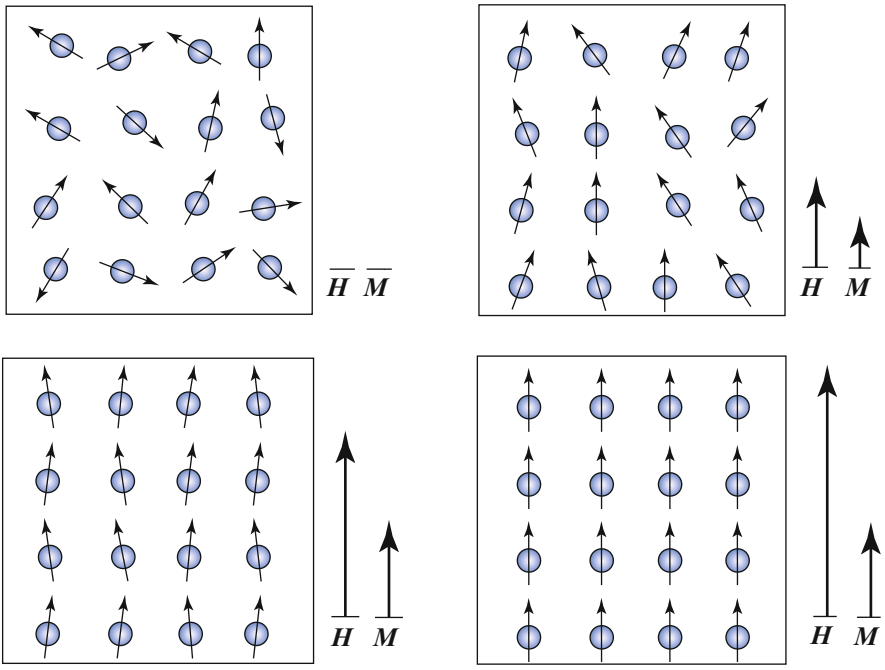

Fig. 2.5 Magnetic behavior of superparamagnetic nanoparticles in an applied magnetic field $\boldsymbol{H}$. Shown are the magnetic moments of the particles, the applied magnetic field as well as the resulting net magnetization. As can be seen in the *second row*, at a certain field strength, the majority of particles is aligned with the magnetic field such that the magnetization remains in saturation for increasing field strength

The relation between the external magnetic field and the length of the particles magnetization is not linear but exhibits nonlinear parts as is shown in Fig. 2.6. The magnetization shows a sharp increase, as the external field increases from zero. At a certain field strength, the magnetization flattens and goes into *saturation*. This is due to the fact that the majority of particles is aligned with the magnetic field such that the maximum magnetization is reached (see Fig. 2.5). Increasing the field strength beyond this point will not change the particle magnetization, which will play a major role for spatial encoding in Sect. 2.4. The magnetization curve can be basically divided into a dynamic part, for which a field deviation is attended by a magnetization change, and a saturation part, for which the magnetization is constant even when the applied field changes.

Mathematically, the saturation effect describing the particle magnetization can be modeled using the Langevin function

$$\mathcal{L}(\xi) := \begin{cases} \left(\coth(\xi) - \frac{1}{\xi}\right) & \xi \neq 0 \\ 0 & \xi = 0 \end{cases}. \tag{2.5}$$

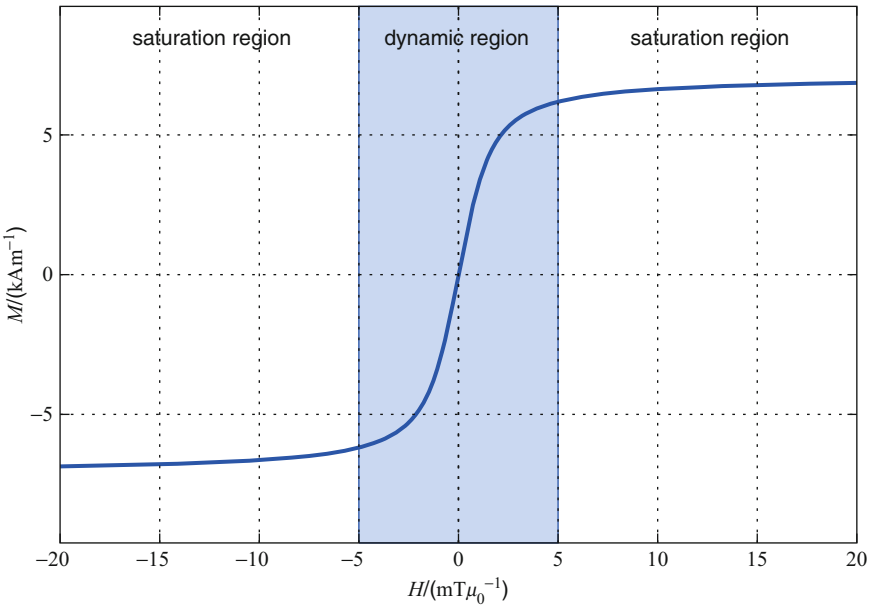

Fig. 2.6 The relation between the external magnetic field (usually measured in A/m or $\mathrm{mT}\mu_0^{-1}$)[1] and the magnetization of the particles for $D = 30\,\mathrm{nm}$ particle diameter and unit iron concentration. If the external field is small, the particles are not yet in saturation, and the magnetization shows a sharp increase. For larger external fields, the particle goes into saturation, and the magnetization hardly changes with the external field

The dependency of the particles' magnetization length M on the magnetic field is then described by

$$M(H) = c\, m \mathcal{L}(\beta H) \tag{2.6}$$

with

$$\beta := \frac{\mu_0 m}{k_\mathrm{B} T^\mathrm{P}}. \tag{2.7}$$

Here, k_B denotes the Boltzmann constant, T^P denotes the particle temperature, μ_0 denotes permeability of free space and $m := \|\boldsymbol{m}\|_2$ denotes the modulus of the magnetic moment of a single particle.

[1]Field strengths are reported in units of $\mathrm{T}\mu_0^{-1} = 4\pi\ \mathrm{Am}^{-1}$ in this book. This convention has been introduced in the first MPI publication [GW05] and since that time consistently used in most MPI-related publications. The aim of this convention is to report the numbers on a Tesla scale, which most readers with a background in MRI are familiar with, but, on the other hand still use the correct unit for the magnetic field strength.

In (2.6), the Langevin function is multiplied with the particle concentration c and the particle magnetic moment m. The latter can be calculated as follows:

$$m = VM_{\text{core}}^{\text{S}}. \tag{2.8}$$

Here, $M_{\text{core}}^{\text{S}}$ is the saturation magnetization of the material the particle core is made of and V is the particle core volume. The volume of a spherical particle with core diameter D is given by

$$V = \frac{1}{6}\pi D^3. \tag{2.9}$$

To discuss the impact of c and m on the magnetization, one has to take into account that in practice the iron concentration and not the particle concentration is the limiting factor for the application of particles in vivo. For constant iron concentration, the particle concentration scales inversely with the particle volume, i.e., $c \propto V^{-1}$. Consequently, for constant iron concentration, the scaling factor $c\,m$ in front of the Langevin function in (2.6) and in turn the saturation magnetization of the suspension

$$M^{\text{S}} = c\,m \tag{2.10}$$

is independent of the particle size. This is graphically supported in Fig. 2.7, where the magnetization characteristic is shown for different particle diameters but constant (unit) iron concentration.

Besides the scaling of the Langevin function, an important property of the magnetization characteristic is the field strength at which the saturation region of the magnetization is reached. This is named the *saturation field strength*. It is, however, not uniquely defined as actually full saturation is only achieved when applying an infinite field strength. One possible way is to define the saturation field strength H^{S} as that field strength for which the magnetization reaches 80% of the saturation magnetization. The Langevin function reaches a value of 0.8 at about $\xi^{\text{S}} = 5$. Due to the scaling of the field strength with the factor β in (2.6), the saturation field strength varies in dependence of β, i.e.,

$$H^{\text{S}} = \frac{\xi^{\text{S}}}{\beta} = \frac{5k_{\text{B}}T^{\text{P}}}{\mu_0 m}. \tag{2.11}$$

In Fig. 2.7, magnetization characteristics for different particle diameters are plotted. As the magnetic moment m scales with the third power of the particle diameter, the saturation field strength scales with the reciprocal of D^3. This means that large particles have a low saturation field strength while small particles have high saturation field strength. Therefore, smaller particles need a higher field strength to get into the state of saturation than larger particles. As it will be discussed in

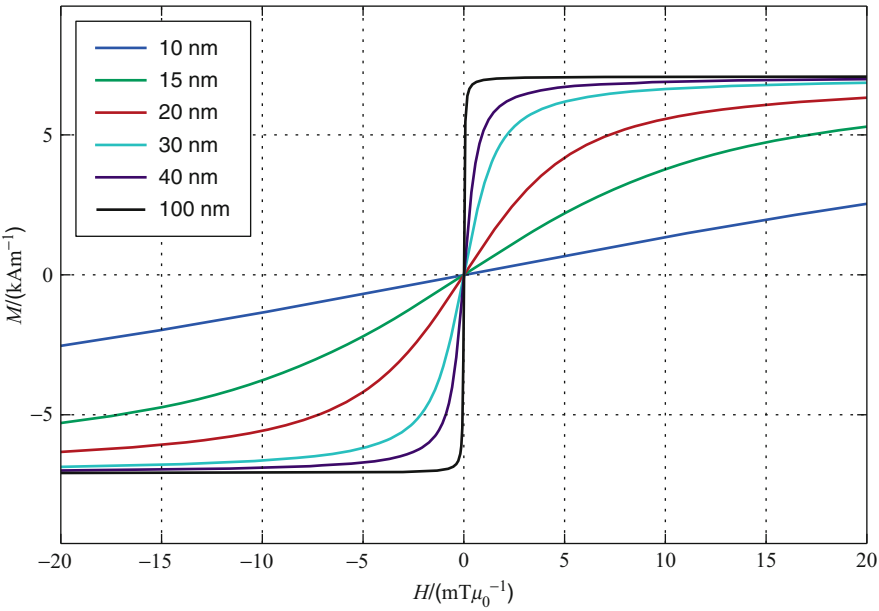

Fig. 2.7 Particle magnetization M as a function of the applied field strength H for different particle core diameters D and unit iron concentration

Sect. 2.7.1, the lower the saturation field strength, the higher is the spatial resolution. Thus a low saturation field strength and, in turn, a large particle size is advantageous in MPI. In the limit $D \to \infty$, the magnetization curve approaches a step function, which can be seen as the ideal magnetization characteristic for MPI.

In practice, the maximum sensible particle size is limited by different factors. First, as will be discussed in Sect. 2.2.6, large particles suffer from relaxation effects, which means that the particles react on a field variation only after a certain amount of time. This puts a limit on the applicable frequency of the applied oscillating magnetic field and, in turn, the signal-to-noise ratio (SNR) of the measurement signal. Second, there are several medical applications, such as the sentinel lymph node biopsy, which favor small particles as these travel to specific parts within the human body, which larger particles do not enter.

2.2.3 Derivative of the Magnetization Characteristic

A different approach to analyze the width of the dynamic range of the magnetization characteristic is to consider the derivative of the magnetization given by

$$M'(H) = c\, m\beta \mathcal{L}'(\beta H)\,, \tag{2.12}$$

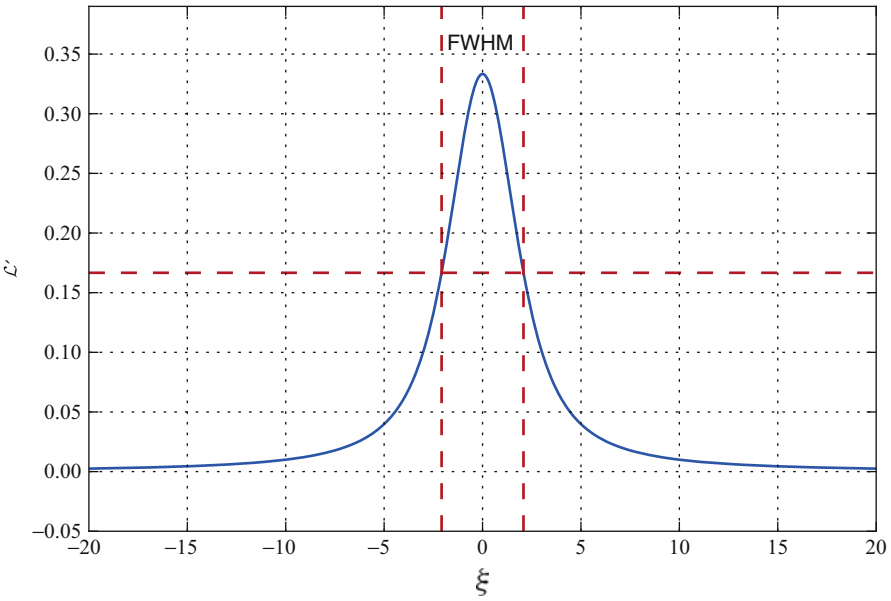

Fig. 2.8 Derivative of the Langevin function $\mathcal{L}'$. The *vertical dashed red lines* indicate the FWHM of $\mathcal{L}'$

where

$$\mathcal{L}'(\xi) = \begin{cases} \left(\frac{1}{\xi^2} - \frac{1}{\sinh^2(\xi)}\right) & \xi \neq 0 \\ \frac{1}{3} & \xi = 0 \end{cases} \tag{2.13}$$

is the derivative of the Langevin function. In Fig. 2.8, the derivative of the Langevin function is shown. As can be seen, the derivative has a maximum at $\xi = 0$ and then decreases rapidly to zero for increasing ξ. In the saturation region, obviously, the derivative of the Langevin function is almost zero.

The width of the dynamic range of the magnetization characteristic can be alternatively reported using the full width at half maximum (FWHM) of its derivative M'. The FWHM is defined as the width at which a kernel function decays to 50% of its maximum. For the derivative of the Langevin function, the FWHM is approximately given by

$$\Delta\xi^{\mathrm{FWHM}} = 4.16. \tag{2.14}$$

The FWHM of the derivative of the magnetization characteristic is in turn given by

$$\Delta H^{\mathrm{FWHM}} = \frac{\Delta\xi^{\mathrm{FWHM}}}{\beta} = \frac{4.16\, k_{\mathrm{B}} T^{\mathrm{P}}}{\mu_0 m}. \tag{2.15}$$

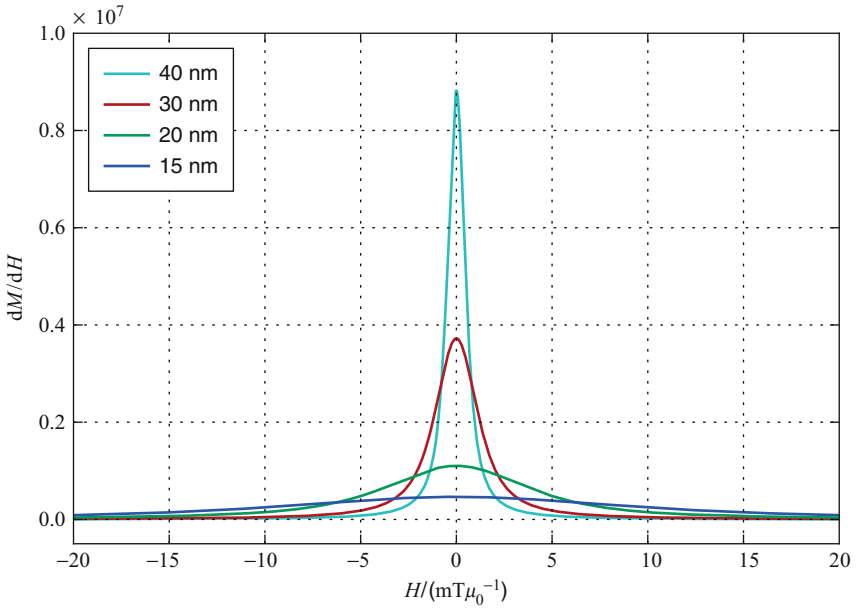

Fig. 2.9 Derivative of the particle magnetization as a function of the applied field strength H for different particle core diameters D and unit iron concentration

While the width of the dynamic range affects the spatial resolution, the signal-to-noise ratio of the induced signal is linked to the steepness of the magnetization curve, which can be measured by the highest slope of the magnetization characteristic, i.e., the peak of the derivative of the magnetization at field strength zero:

$$M'(0) = c\, m \frac{\beta}{3} = c\, m \frac{\mu_0 m}{3 k_\mathrm{B} T^\mathrm{P}}. \tag{2.16}$$

In Fig. 2.9, the derivative of the magnetization characteristic is shown for different particle diameters and constant iron concentration. As can be seen, the height of the kernel scales with D^3 while the width of the kernel is inversely proportional to D^3. Mathematically this can be verified by inspection of (2.15) and (2.16) where one has to keep in mind that the product $c\, m$ is constant for constant iron concentration (see Sect. 2.2.2).

2.2.4 Mean Magnetic Moment

The magnetization $\boldsymbol{M}$ depends on the applied magnetic field $\boldsymbol{H}$ but also on the particle concentration c. As the aim of MPI is to determine the particle concentration, it

is convenient to separate the concentration c from the magnetization $\boldsymbol{M}$ in the form

$$\boldsymbol{M} = c\overline{\boldsymbol{m}}. \tag{2.17}$$

Here, $\overline{\boldsymbol{m}}$ denotes the mean magnetic moment that is defined as

$$\overline{\boldsymbol{m}} := \frac{1}{N^{\mathrm{P}}} \sum_{j=0}^{N^{\mathrm{P}}-1} \boldsymbol{m}_j. \tag{2.18}$$

The linear dependency of the magnetization on the particle concentration c can be derived by inserting (2.1) into (2.2). As it is discussed in Chap. 4, the reconstruction principle applied in MPI is based on the linear relationship between the particle magnetization and the particle concentration.

2.2.5 Particle Size Distribution

Until now it has been assumed that all particles within the particle suspension are of the same size. In practice, it is a challenging task to develop a tracer, which consists of monosized particles. Instead, there are particles of different size in the suspension. The size distribution of the nanoparticles can be described by the probability density function (PDF) $\rho(D)$. For a monodisperse particle distribution with a particle size D', the PDF is given by

$$\rho(D) = \delta(D - D'), \tag{2.19}$$

where δ is the Dirac delta distribution. In theory, the PDF of a polydisperse size distribution can have an arbitrary shape with the restriction that

$$\rho(D) = 0 \quad \text{for} \quad D \leq 0. \tag{2.20}$$

This is obviously necessary as particles with a negative particle diameter cannot exist. Assuming a natural growth process, the PDF follows a log-normal distribution [KSNG99]

$$\rho(D) = \begin{cases} \dfrac{1}{\tilde{\sigma} D \sqrt{2\pi}} \exp\left(-\dfrac{1}{2} \left(\dfrac{\ln(D) - \tilde{\mu}}{\tilde{\sigma}} \right)^2 \right) & D > 0 \\ 0 & D \leq 0 \end{cases}. \tag{2.21}$$

Here, the parameters $\tilde{\mu}$ and $\tilde{\sigma}$ are related to the expectation value $\mathrm{E}(D)$ and the standard deviation $\sqrt{\mathrm{Var}(D)}$:

$$\tilde{\mu} = \ln(\mathrm{E}(D)) - \frac{1}{2} \ln\left(\frac{\mathrm{Var}(D)}{\mathrm{E}^2(D)} + 1 \right), \tag{2.22}$$

$$\tilde{\sigma} = \sqrt{\ln\left(\frac{\mathrm{Var}(D)}{\mathrm{E}^2(D)} + 1 \right)}. \tag{2.23}$$

In Fig. 2.10, several log-normal distributions are plotted for different $\mathrm{E}(D)$ and $\sqrt{\mathrm{Var}(D)}$. As can be seen in the upper plot, the log-normal distribution approaches an ordinary normal distribution if the expectation value is several times larger than the standard deviation. Furthermore, in the lower plot, it can be observed that the expectation value does not correspond with the maximum of the PDF. This is due to the asymmetry of the PDF with regard to the maximum.

2.2.6 Relaxation Effects

Until now it has been assumed that the particles are always in thermal equilibrium. In this case both the magnetic field vector $\boldsymbol{H}$ and the magnetization vector $\boldsymbol{M}$ have the same direction. This is strictly true only if the applied magnetic field is static. When considering a time-varying magnetic field, the particle magnetization vector follows the direction of the applied field with a certain delay. Also, the change in the magnetization magnitude will happen a little later than the change in the magnetic field strength. This delay can be described by the relaxation time τ and leads to an open hysteresis loop in the magnetization curve. Considering a magnetic field that is first static and then instantaneously vanishes, the particle magnetization magnitude will decrease exponentially with the relaxation time τ:

$$M^{\mathrm{R}}(t) = M(0) \exp\left(-\frac{t}{\tau}\right). \tag{2.24}$$

Here, $M(0)$ is the magnetization when the magnetic field is turned off and $M^{\mathrm{R}}(t)$ is the remanent magnetization at time $t > 0$.

Whether relaxation effects have to be taken into account depends highly on the frequency of the applied magnetic fields f^{E}. If the change of the magnetic field is slow enough for the magnetization to follow the magnetic field, i.e., when

$$f^{\mathrm{E}} \ll \frac{1}{\tau}, \tag{2.25}$$

relaxation effects can be neglected and the particle magnetization follows in good approximation the Langevin function described in Sect. 2.2.2 even for dynamic fields. If the applied frequency is in the range of $\frac{1}{\tau}$, hysteresis effects occur and characterization of the particle magnetization is considerably more complicated. Still, the MPI method can be applied although the theory and the concepts introduced in this chapter are simplifications and hold only up to a certain accuracy. When increasing the frequency further, at some point, the particle magnetization cannot follow the change of the magnetic field anymore and will therefore drastically lose amplitude. Therefore, the MPI method will fail if the applied frequency is too high.

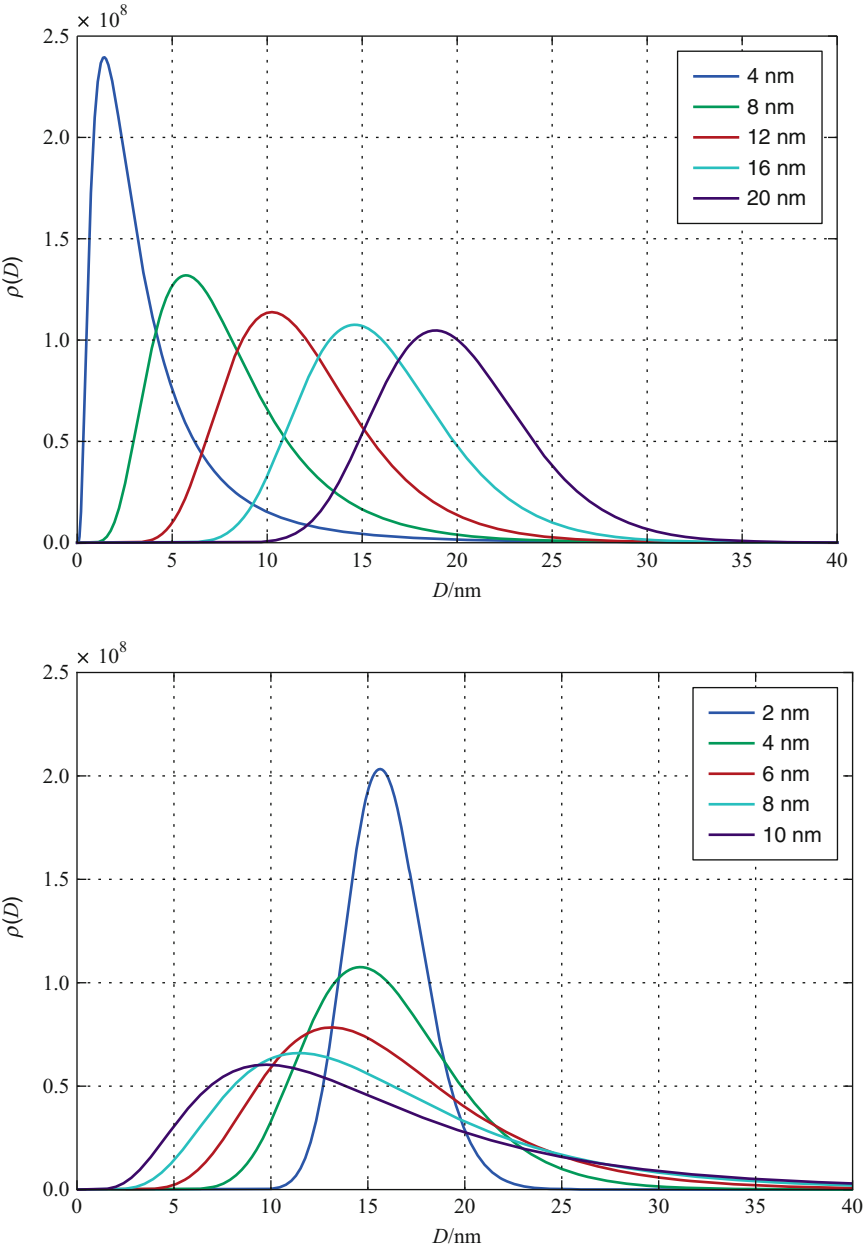

Fig. 2.10 Several log-normal distributions for different expectation values and standard deviations. In the *upper plot*, the standard deviation is 4 nm and the expectation value is varied. In the *lower plot*, the expectation value is 16 nm and the standard deviation is varied

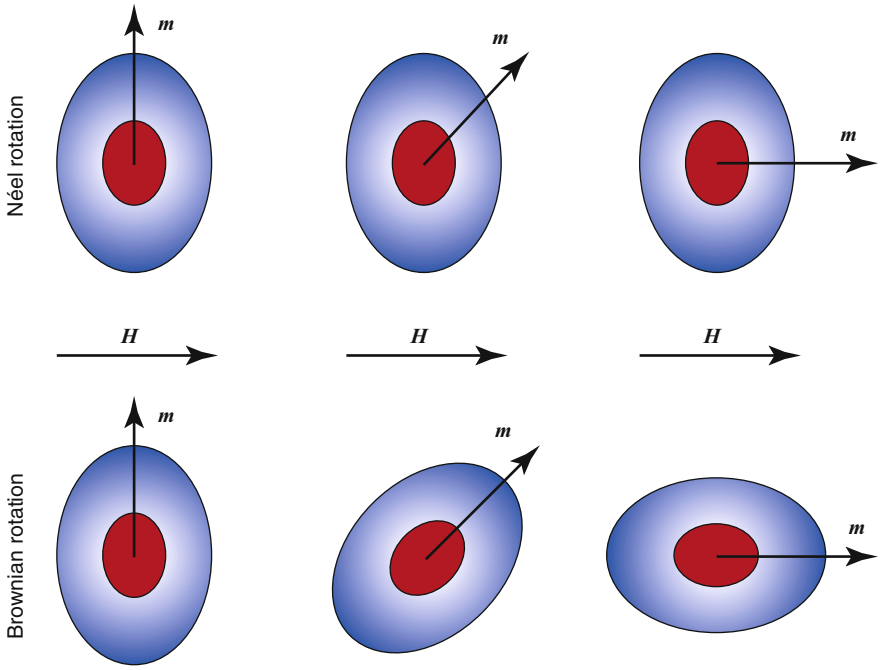

Fig. 2.11 Comparison of Néel and Brownian rotation. While Néel rotation describes a rotation of the particles' magnetic moment for a fixed particle, Brownian rotation describes a mechanical rotation of the entire particle

The concepts and theories developed and discussed in this book are restricted to applied frequencies, which are lower than the reciprocal particle relaxation times. Although in some MPI-related publications, simple models including relaxation effects have been considered [FMK09, FKMK11], the Langevin theory is still the standard model used to date.

There are, in general, two ways a magnetic nanoparticle can change its direction when the applied field changes temporarily. Either the particle itself performs a physical rotation, which is named Brownian rotation, or the magnetic moment in the particle can rotate in a fixed particle, which is named Néel rotation. In a viscose medium, a combination of both rotations is performed and it depends on the applied frequency, which process is the dominant one. In Fig. 2.11, Néel and Brownian rotation are compared.

The relaxation time of the Néel rotation can be computed by

$$\tau^{\mathrm{N}} = \tau_0 \exp\left(\frac{K^{\mathrm{A}} V}{k_{\mathrm{B}} T^{\mathrm{P}}}\right), \tag{2.26}$$

where K^{A} is the anisotropy constant [N49, N55] and V is the particle core volume. The relaxation time of Brownian rotation can be computed by

$$\tau^{\mathrm{B}} = \frac{3\eta V^{\mathrm{H}}}{k_{\mathrm{B}} T^{\mathrm{P}}}. \tag{2.27}$$

Here, η is the viscosity of the fluid and V^{H} is the hydrodynamical volume [Bro63]. In contrast to the Néel relaxation time, which depends exponentially on the (core) particle volume, the Brownian relaxation time linearly depends on the (hydrodynamical) particle volume. Hence, in the lower frequency range, the Brownian relaxation will dominate if the suspension is sufficiently viscose, while in the higher frequency range Néel relaxation will be dominant. The total relaxation time is a combination of the Néel and the Brownian relaxation times and can be approximated by

$$\tau = \frac{\tau^{\mathrm{B}} \tau^{\mathrm{N}}}{\tau^{\mathrm{B}} + \tau^{\mathrm{N}}}. \tag{2.28}$$

Hence, the shorter of both relaxation times determines the total relaxation time. The transition frequency between Néel and Brownian depends on the particle size, the particle anisotropy, and the viscosity of the particle suspension.

2.3 Signal Generation and Acquisition

Following the discussion of the magnetization behavior of magnetic nanoparticles, this section will discuss, how the particles can be excited such that they respond with a characteristic signal. Beforehand, the reception of the particle magnetization using the induction principle is investigated.

2.3.1 Signal Reception

In its very basic form, MPI applies a time-dependent external magnetic field to change the magnetization of the magnetic material using *send coils*. In order to detect the change of the magnetization, one needs a method to measure the magnetic flux density. In MPI this is done by measuring the voltage induced in *receive coils*. The inductive measurement is mainly used due its ability to measure very small magnetization changes at high frequencies in the kHz–MHz range, which are typically used in MPI.

2.3.1.1 Induction Principle

The induction principle is, as the name indicates, linked to Faraday's law of induction, which is given in differential form by

$$\nabla \times \boldsymbol{E} = -\frac{\partial \boldsymbol{B}}{\partial t}. \tag{2.29}$$

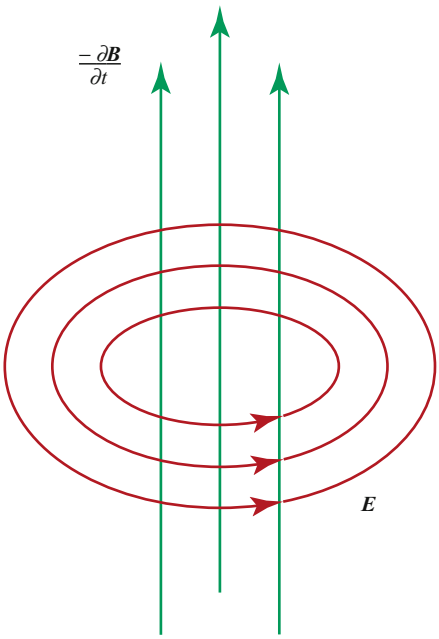

Fig. 2.12 Induction principle: The temporal change of the magnetic flux density causes an electric field along concentric trajectories around the axis of the magnetic flux density

Here, $\boldsymbol{E}$ is the electric field strength and

$$\boldsymbol{B} = \mu_0(\boldsymbol{H} + \boldsymbol{M}), \tag{2.30}$$

is the magnetic flux density (see Appendix A). Faraday's law of induction states that there establishes an electrical field, whenever the magnetic flux density changes temporarily. The field lines of the electrical field travel along concentric trajectories around the magnetic flux axis. This is graphically supported in Fig. 2.12. In integral form, Faraday's law of induction can be equivalently written as

$$\oint_{\partial S} \boldsymbol{E}(\boldsymbol{l}) \cdot \mathrm{d}\boldsymbol{l} = -\frac{\mathrm{d}}{\mathrm{d}t}\Phi_S^{\boldsymbol{B}}, \tag{2.31}$$

where S is a surface and

$$\Phi_S^{\boldsymbol{B}} = \int_S \boldsymbol{B}(\boldsymbol{r}) \cdot \mathrm{d}\boldsymbol{A} \tag{2.32}$$

is the magnetic flux through the surface.

2.3.1.2 Magnetic Flux Through a Receive Coil

Now let us consider a receive coil consisting for simplicity of a single conductor loop enclosing a surface S. The voltage at the end points of the receive coil is, by

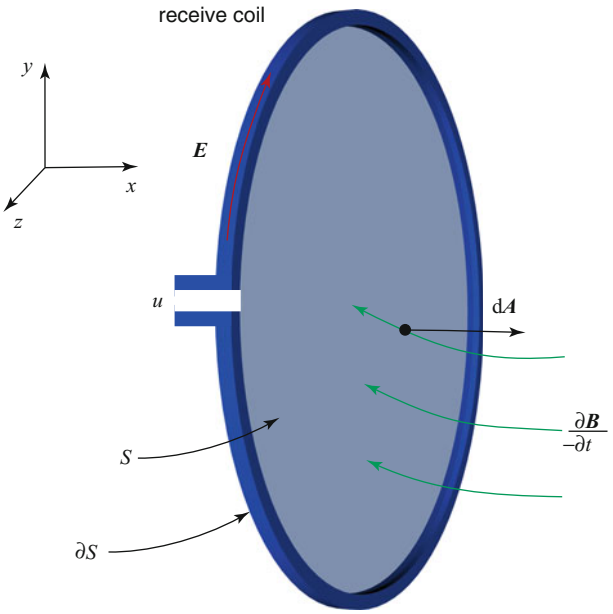

Fig. 2.13 Voltage induced in a receive coil, which spans a surface S. The surface integral of the temporal deviation of the magnetic flux density $\boldsymbol{B}$ is equal to the line integral of the electric field $\boldsymbol{E}$ along the conductor, which is the voltage u that can be measured at the end points

definition, the integration of the electric field strength along the conductor, i.e.,

$$u(t) = \oint_{\partial S} \boldsymbol{E}(\boldsymbol{l}, t) \cdot \mathrm{d}\boldsymbol{l}. \tag{2.33}$$

Comparing this integral, with the left-hand side of the integral form of Faraday's law of induction (2.31), one can see that the voltage measured in the receive coil is equal to the negative of the time derivative of the magnetic flux, i.e.,

$$u(t) = -\frac{\mathrm{d}}{\mathrm{d}t} \Phi_S^{\boldsymbol{B}}(t). \tag{2.34}$$

By inserting the definition of the magnetic flux, one derives

$$u(t) = -\frac{\mathrm{d}}{\mathrm{d}t} \int_S \boldsymbol{B}(\boldsymbol{r}, t) \cdot \mathrm{d}\boldsymbol{A}. \tag{2.35}$$

Hence, the voltage induced in the receive coil is the integration of the magnetic flux density $\boldsymbol{B}$ over the surface spanned by the receive coil. The differential vector $\mathrm{d}\boldsymbol{A}$ is directed perpendicularly to the surface. Hence, the product $\boldsymbol{B}(\boldsymbol{r}, t) \cdot \mathrm{d}\boldsymbol{A}$ is equal to the length of the magnetic flux density vector in direction of the outer normal of the receive coil surface (Fig. 2.13).

Due to the time derivative on the right-hand side of (2.35), it is only the variation of the magnetization $\frac{\partial \boldsymbol{M}}{\partial t}$ that can be detected using electromagnetic induction. This is, however, not a drawback of the induction method as it is not the particle dynamics, which MPI aims to image but the particle concentration. The latter can be factored out of the magnetization change $\frac{\partial \boldsymbol{M}}{\partial t}$ due to the linear dependency described in Sect. 2.2.2.

2.3.1.3 Detection of the Particle Magnetization

To determine the voltage induced by the superparamagnetic nanoparticles in a receive coil one has to compute the magnetization within the enclosed surface of the receive coil (2.35). As it is derived in Appendix A.4.3, there is an alternative way to express the induced voltage using the law of reciprocity [HR76], which leads to an integration over the volume, where the particles are located, i.e. the object to be imaged. The induced voltage is then given by

$$\begin{aligned} u^{\mathrm{P}}(t) &= -\mu_0 \frac{\mathrm{d}}{\mathrm{d}t} \int_{\text{object}} \boldsymbol{p}^{\mathrm{R}}(\boldsymbol{r}) \cdot \boldsymbol{M}(\boldsymbol{r}, t) \mathrm{d}^3 r \\ &= -\mu_0 \int_{\text{object}} \boldsymbol{p}^{\mathrm{R}}(\boldsymbol{r}) \cdot \frac{\partial \boldsymbol{M}(\boldsymbol{r}, t)}{\partial t} \mathrm{d}^3 r, \end{aligned} \tag{2.36}$$

where $\boldsymbol{p}^{\mathrm{R}}(\boldsymbol{r})$ denotes the receive coil sensitivity, which contains all geometrical parameters of the coil, for instance, the path of the wire determining the size of the enclosed surface S. The coil sensitivity is essentially the magnetic field that would be generated by the coil if driven by unit current, i.e.,

$$\boldsymbol{p}^{\mathrm{R}}(\boldsymbol{r}) := \frac{\boldsymbol{H}^{\mathrm{R}}(\boldsymbol{r})}{I^{\mathrm{R}}}. \tag{2.37}$$

The law of reciprocity states that the receiving properties of a coil are the same as the field generating properties. This knowledge is essential when designing the coils of an MPI scanner. Both the send and the receive coils should be designed to have a high sensitivity: the send coils to minimize the power loss of the setup, the receive coils to maximize the SNR of the measured signal. To pick up the particle magnetization at all positions in the FOV, ideally, the receive coil sensitivity should be homogeneous in space.

2.3.2 Direct Coupling of Excitation Field

In order to get the particles to induce a voltage signal in the receive coils, a dynamic field excitation is needed. The dynamic magnetic field directly couples into the receive coil and induces according to (2.35) a respective excitation signal:

$$u^{\mathrm{E}}(t) = -\mu_0 \frac{\mathrm{d}}{\mathrm{d}t} \oint_{\partial S} \boldsymbol{H}(\boldsymbol{r}, t) \cdot \mathrm{d}\boldsymbol{A}. \tag{2.38}$$

The voltage measured in the receive coil is the superposition of the particle signal u^{P} induced by the time-varying magnetization and the excitation signal u^{E} induced by the time-varying magnetic field, i.e.,

$$u(t) = u^{\mathrm{P}}(t) + u^{\mathrm{E}}(t). \tag{2.39}$$

To determine the particle distribution c one needs a way to access the particle signal $u^{\mathrm{P}}(t)$. From a mathematical perspective, this seems to be feasible and could be solved by performing the following steps:

1. Measure the signal induced by the excitation field in an empty scanner:

$$u^{\mathrm{empty}}(t) = u^{\mathrm{E}}(t) \tag{2.40}$$

2. Perform the regular MPI measurement:

$$u(t) = u^{\mathrm{E}}(t) + u^{\mathrm{P}}(t) \tag{2.41}$$

3. Extract the particle signal by subtracting the empty measurement:

$$u^{\mathrm{P}}(t) = u(t) - u^{\mathrm{empty}}(t) \tag{2.42}$$

Unfortunately, this obvious procedure is only feasible in theory when all signals are available at infinite precision. In practice, the particle signal u^{P} is very small compared to the induced excitation signal u^{E}. For typical particle concentrations and coil sensitivities, the particle signal is more than six orders of magnitude lower than the induced excitation signal. On top of that, as is discussed in Sect. 2.3.4, the particle signal itself has a high dynamic range of several decades such that there are frequency components, which have an amplitude 10^{10} times lower than the excitation signal.

To convert the analog signal into a digital signal, one uses an analog-to-digital converter (ADC). Even advanced ADCs have a finite input range of about 16 bits at the frequency range used in MPI. Hence, the ADC can only resolve a range of about 10^5 V.

Now, what would happen if one tries to digitize the voltage $u(t)$ and remove the excitation signal $u^{\mathrm{E}}(t)$? One would obtain a signal containing no particle signal but only quantization noise. This shows that one cannot get rid of the excitation signal by simple post-processing of the data. Instead, one has to choose the excitation signal in a special way such that it can be filtered prior to digitization. Therefore, the signals u^{E} and u^{P} have to be distinguishable.

2.3.3 Signal Generation

Now that we know that it requires a time-varying magnetization to detect the magnetization change using receive coils, we have to choose the dynamic magnetic field that is used to excite the particles. As we have seen in the last section, the

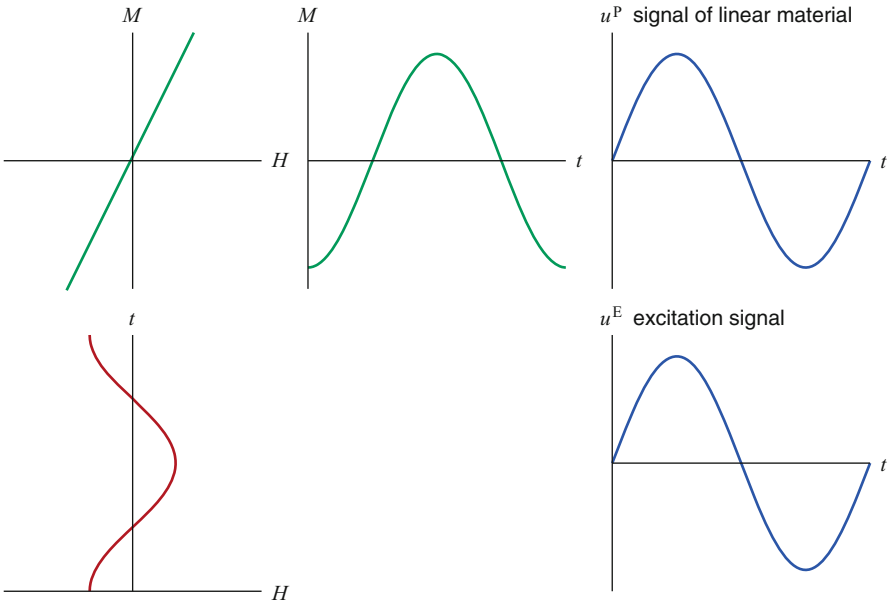

Fig. 2.14 Magnetization progression and induced signals for a linear material and sinusoidal field excitation. As the magnetization characteristic is linear, both the induced magnetization signal and the induced excitation signal resemble a sinusoidal function and cannot be distinguished

temporal progression of the magnetic field has to be chosen such that both the induced particle signal and the induced excitation signal can be distinguished. Actually, this can be achieved by selecting an excitation field of a very small bandwidth, for instance, a sinusoidal excitation field[2]

$$H^{\mathrm{E}}(t) = -A^{\mathrm{E}} \cos(2\pi f^{\mathrm{E}} t), \tag{2.43}$$

where A^{E} denotes the amplitude and f^{E} denotes the frequency of the field. The repetition time for one field cycle is given by $T^{\mathrm{R}} = \frac{1}{f^{\mathrm{E}}}$. The excitation field is usually homogeneous in space such that all particles within the volume of interest experience the same field. The field is, however, not required to be as homogeneous as the B_0 field in MRI.

Assuming for a moment that the relation between the external field and the magnetization of the particles would be linear, the magnetization progression would resemble the waveform of the external field and would be purely sinusoidal. Hence, there would be no way to distinguish the voltage induced by the external field and the voltage induced by the particle magnetization (see Fig. 2.14).

[2]Note that the cosine excitation is considered to simplify later calculations.

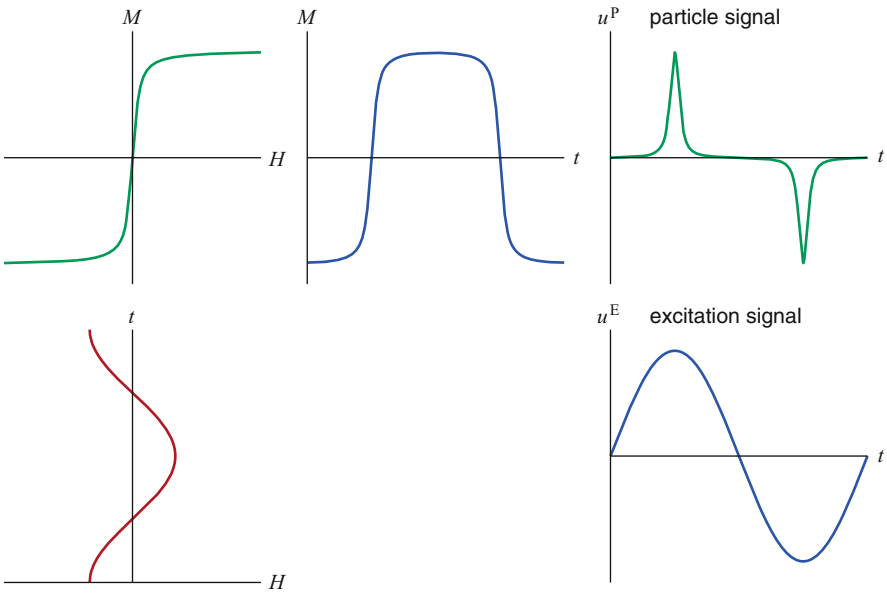

Fig. 2.15 Signal generation in MPI: The magnetic nanoparticles are excited with a sinusoidal magnetic field causing a magnetization progression, which resembles a rectangular function. The induced voltage contains two sharp peaks and can be distinguished from the sinusoidal excitation signal directly coupling into the receive coil

But, as the relationship between the external field and the particle magnetization is nonlinear, both signals can be discriminated. As it is shown in Fig. 2.15, the magnetization progression resembles that of the external field only for small field strength and approaches a constant function when the external field proceeds to higher field strengths. One might say that the sinusoidal progression is cut off when the magnetization reaches its maximum value. Actually, the magnetization progression has more similarities with a rectangular function than with a sinusoidal one. In fact, for a step-like magnetization characteristic, the magnetization progression would be exactly rectangular as the magnetization would only flip its direction, when the external field changes in sign.

Considering the induced voltage, one can see in Fig. 2.15 that there are two peaks in the signal. These occur whenever the magnetization rapidly changes, which is the case when the particle flips its direction. In Sect. 2.4, it is shown that this behavior is the key to achieve spatial encoding in MPI. The more pronounced the difference between the applied sinusoidal excitation field and the magnetization progression is, the steeper is the magnetization curve. Later in this book, it is shown that a low saturation field strength ensures a high spatial resolution. Hence, a step-like magnetization curve is indeed the ideal situation for imaging with MPI. In this ideal case, the induced voltage signal would contain exactly two Dirac delta peaks per period and would be zero elsewhere.

2.3.4 Signal Spectrum

To study the differences between the excitation signal and the particle signal, it is instructive to consider both signals in frequency space. Due to the periodicity of the field excitation, the induced excitation signal and the induced particle signal are periodic as well. Hence, these signals can be expanded into a Fourier series

$$u(t) = \sum_{k=-\infty}^{\infty} \hat{u}_k \mathrm{e}^{2\pi \mathrm{i} k f^{\mathrm{E}} t} \tag{2.44}$$

and the spectrum consists of discrete lines at multiples of the frequency f^{E}, which is also called the fundamental or base frequency. These multiples,

$$f_k = k f^{\mathrm{E}}, \quad k \in \mathbb{Z}, \tag{2.45}$$

are usually called harmonic frequencies or just harmonics. The Fourier coefficients can be computed by

$$\hat{u}_k = \frac{1}{T^{\mathrm{R}}} \int_0^{T^{\mathrm{R}}} u(t) \mathrm{e}^{-2\pi \mathrm{i} k f^{\mathrm{E}} t} \, \mathrm{d}t, \quad k \in \mathbb{Z}. \tag{2.46}$$

As the induced voltage is real, the Fourier coefficients obey the relation

$$\begin{aligned} \hat{u}_k &= \frac{1}{T^{\mathrm{R}}} \int_0^{T^{\mathrm{R}}} u(t) \mathrm{e}^{-2\pi \mathrm{i} k f^{\mathrm{E}} t} \, \mathrm{d}t \\ &= \frac{1}{T^{\mathrm{R}}} \int_0^{T^{\mathrm{R}}} \left(u(t) \mathrm{e}^{2\pi \mathrm{i} k f^{\mathrm{E}} t} \right)^* \mathrm{d}t \\ &= (\hat{u}_{-k})^* . \end{aligned} \tag{2.47}$$

Therefore, one usually neglects the negative frequencies in MPI as they do not carry any additional information.

Being a purely sinusoidal function, the excitation signal shows up as a single peak at the frequency f^{E}. Due to the nonlinear relationship between magnetization and external field, the particle signal has not only a peak at the fundamental frequency but rather at all higher harmonics. This is shown in Fig. 2.16, where the periodic particle signal and its Fourier transform are shown.

The generation of higher harmonics for a nonlinear magnetization curve can be mathematically described by expanding the Langevin function into a Taylor series

$$\mathcal{L}(\xi) = \frac{1}{3}\xi - \frac{1}{45}\xi^3 + \frac{2}{954}\xi^5 - \frac{1}{4{,}725}\xi^7 + \dots . \tag{2.48}$$

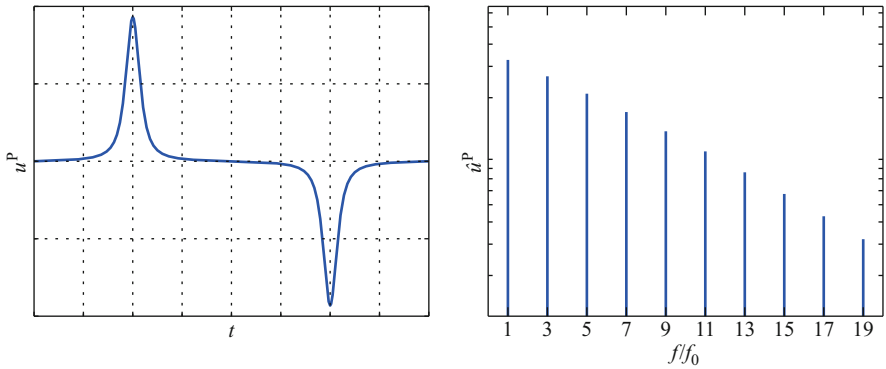

Fig. 2.16 Induced particle signal for sinusoidal excitation (*left*) and the respective Fourier coefficients on a logarithmic scale (*right*)

If one considers the particle magnetization M, one can see that the argument $\frac{\mu_0 Hm}{k_{\mathrm{B}}T^{\mathrm{P}}}$ is applied to the Langevin function. For a sinusoidal field excitation $H(t) = -A^{\mathrm{E}}\cos(2\pi f^{\mathrm{E}}t)$, the dynamic part of the particle magnetization can be written as

$$\mathcal{L}\left(\tilde{\xi}\cos\left(2\pi f^{\mathrm{E}}t\right)\right) = \frac{\tilde{\xi}}{3}\cos\left(2\pi f^{\mathrm{E}}t\right) - \frac{\tilde{\xi}^3}{45}\cos^3\left(2\pi f^{\mathrm{E}}t\right) + \ldots, \tag{2.49}$$

where $\tilde{\xi} = -\frac{\mu_0 A^{\mathrm{E}} m}{k_{\mathrm{B}}T^{\mathrm{P}}}$. Using the trigonometric formula

$$\cos^3(x) = \frac{1}{4}\left(3\cos(x) + \cos(3x)\right), \tag{2.50}$$

one obtains

$$\begin{aligned}\mathcal{L}\left(\tilde{\xi}\cos(2\pi f^{\mathrm{E}}t)\right) &= \frac{\tilde{\xi}}{3}\cos\left(2\pi f t\right) - \frac{\tilde{\xi}^3}{60}\cos\left(2\pi f^{\mathrm{E}}t\right) + \frac{\tilde{\xi}^3}{180}\cos\left(2\pi(3f^{\mathrm{E}})t\right) + \ldots \\ &= \frac{20\tilde{\xi} - \tilde{\xi}^3}{60}\cos\left(2\pi f^{\mathrm{E}}t\right) + \frac{\tilde{\xi}^3}{180}\cos\left(2\pi(3f^{\mathrm{E}})t\right) + \ldots.\end{aligned} \tag{2.51}$$

Hence, the third harmonic, which corresponds to the frequency $3f^{\mathrm{E}}$ is present in the spectrum of the induced voltage for a sinusoidal excitation. By including higher-order terms $\cos^5$, $\cos^7$, ..., one can verify that all odd harmonics are present in the signal spectrum. The even harmonics are missing, as all even derivatives of the Langevin function have a zero-crossing at the point $\xi = 0$, at which the Taylor series is expanded.

To identify the presence of magnetic material, one only has to look for higher harmonics and ignore the fundamental frequency. In fact, it is a key mechanism

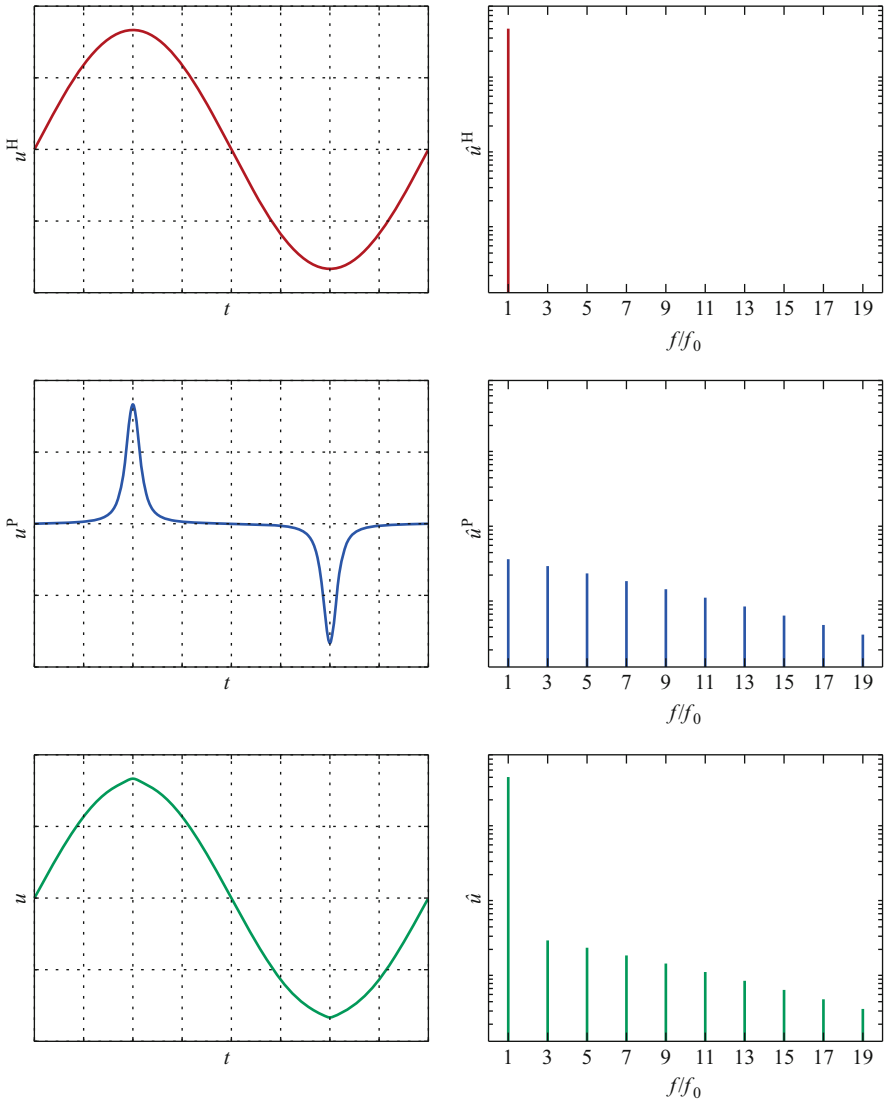

Fig. 2.17 Time signals induced in the receive coil during an MPI experiment for sinusoidal excitation (*left*) and the respective Fourier coefficients on a logarithmic scale (*right*). Besides the induced particle signal (*first row*) and the induced excitation signal (*second row*), the superposition of both signals is shown (*last row*)

to choose an excitation signal with a narrow bandwidth such that the broadband MPI signal is only masked in a narrow frequency band. The remaining unmasked harmonics can be used for imaging. In Fig. 2.17, the signals induced during an MPI experiment are shown in time and frequency space. Besides the particle signal and

the excitation signal, the superposition of both signals is illustrated. As can be seen, the particle signal can hardly be detected in time space. This is due to the low amplitude of the particle signal in comparison to the excitation signal. In contrast, all higher harmonics of the particle signal can be clearly seen in the signal spectrum while only the fundamental frequency is covered by the excitation signal.

Ignoring the fundamental frequency does not only remove the excitation signal but has the additional advantage that it removes any background signal potentially induced by the iron in the human body. As this iron is present in atomic or molecular form and thus substantially smaller than the magnetic nanoparticles, its magnetization characteristic is linear in the considered field range. Hence, the iron only affects the signal at the fundamental frequency (see Fig. 2.14) such that all higher harmonics are background free.

2.3.5 Excitation Frequency and Field Strength

The time-dependent external field that periodically changes the magnetization of the magnetic material usually has a frequency in the range of several tens to over hundreds of kilohertz, with the first results published using a frequency of 25 kHz [GW05]. These frequencies normally are not detectable for the human ear and scanner operation is thus scarcely audible. Using higher frequencies can be beneficial, as the noise in the receiver electronics is in many cases dominated by a $\frac{1}{f}$ behavior. On the contrary, certain physiological limitations apply for the exposure of human bodies to electromagnetic waves, one of those being energy deposition (specific absorption rate, SAR). It is proportional to the square of the field amplitude and frequency [LBF+97], thus posing limitations to the use of higher excitation frequencies. One further limitation is caused by the particles themselves. Due to their finite relaxation times, the particles can only follow a field variation up to a certain frequency. If the excitation frequency is higher, the change of the particle magnetization is suppressed, leading to a loss of intensity of the induced signal.

To be effective, the amplitude of the excitation field should be high enough to ensure that the change in magnetization goes well into the nonlinear areas of the magnetization curve, preferably nearly into saturation. The higher the amplitude, the more pronounced the higher harmonics in the received spectrum of the MPI signal will be. Feasible amplitudes are in the range of several $\mathrm{mT}\mu_0^{-1}$ up to about $20\,\mathrm{mT}\mu_0^{-1}$. Although technically higher amplitudes can be achieved, the SAR limitation leads to a restriction of the excitation field amplitude.

To gain information on the exact amount of magnetic material, i.e., to make a quantitative measurement, it is sufficient to read the amplitude of one selected harmonic from the spectrum. Given a suitable calibration measurement with a well-known amount of magnetic material, the amplitude of the selected harmonic in relation to its value during the calibration measurement will be proportional to the amount of iron. It is, of course, mandatory to keep all parameters, for instance, the field strength of the excitation field, constant between measurements.

2.4 Spatial Encoding: Selection Field

Using a setup as outlined in the last section, i.e., an excitation field with sufficient amplitude that penetrates the volume of interest, one can easily reveal if magnetic material is present or not. However, it is not possible to determine where exactly the magnetic material is and how much material is present at a particular location. What is missing in the explanation up to now is a way to determine the spatial distribution of the magnetic material. This is usually called spatial encoding and the subject of the current section.

2.4.1 Particle Selection

The basic problem of achieving spatial encoding in MPI can be formulated as finding a solution for the task to associate the emitted particle signal to a particular location at a certain time point. In this way, the signal can be directly assigned to the spatial particle concentration. In order to manage that particles at different locations in space generate distinct signals, MPI uses a static magnetic field, which is highly inhomogeneous in space. As is shown in Fig. 2.18, the field in fact has a distinct field vector at each position in space. Furthermore, the field contains one special location named field-free point (FFP), which is simply characterized by the field magnitude or field vector being zero. While veering away from this FFP, the field strength quickly increases in a linear fashion. Such a field is usually called a constant-gradient or, simply, gradient field in the context of magnetic resonance imaging. This name is derived from the gradient being constant for a linear increasing magnetic field.

When applying a gradient field with a strong gradient strength to a volume containing magnetic nanoparticles, the resulting particle magnetization will be in saturation in most positions in space. Only in a small region around the FFP, the particle magnetization will be in the dynamic range of the magnetization curve with zero magnetization at the exact location of the FFP.

When superimposing the excitation field on top of the gradient field, the particles with sufficient distance to the FFP do not react on the change of the total magnetic field (see Fig. 2.19). In turn, almost no MPI signal is induced in the receive coil. In contrast, the particles in close vicinity experience a strong magnetization change with the particles directly located at the FFP flipping back and forth. Actually, at the FFP the particles are only affected by the excitation field and thus behave as described in Sect. 2.3. The magnetization change results in a measurable voltage signal in the receive coil. As this induced signal stems only from the magnetic material in a certain vicinity of the FFP, a direct relation between the signal and the FFP location is established, i.e., spatial encoding is achieved. As the applied gradient field selects the position at which the particles are free to react on a field excitation, it is called *selection field* in the context of MPI.

One thing one has to consider when using the form of spatial encoding outlined above is that the excitation field amplitude should be small compared to the gradient

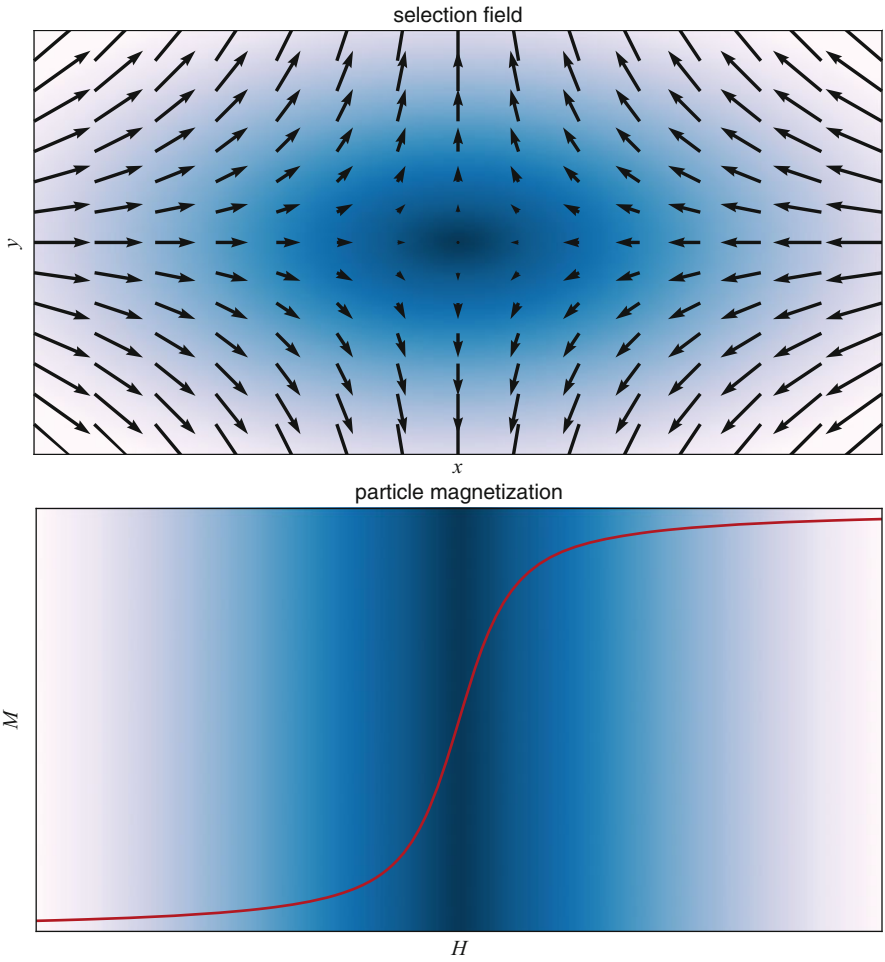

Fig. 2.18 Selection field used for spatial encoding illustrated as a vector plot. In the background, the modulus of the field is shown, where *dark blue* indicates zero field strength and *white* indicates high field strength. The field features a field-free point at the center and increases linearly in all directions in space. The gradient strength in y-direction is twice as high as in x-direction. By comparing the field strengths of the selection field with the particle magnetization curve shown at the *bottom*, it can be seen that only particles in the close vicinity of the FFP are in the unsaturated region of the magnetization curve

of the selection field. Otherwise, the magnetization of saturated particles could be pulled into the dynamic range on the magnetization curve and thus contribute to the measurement signal, which is undesirable. In other words, the excitation field lets the FFP move in space and this movement should not exceed the size of an image voxel, if the goal is to sample a single voxel during each excitation period.

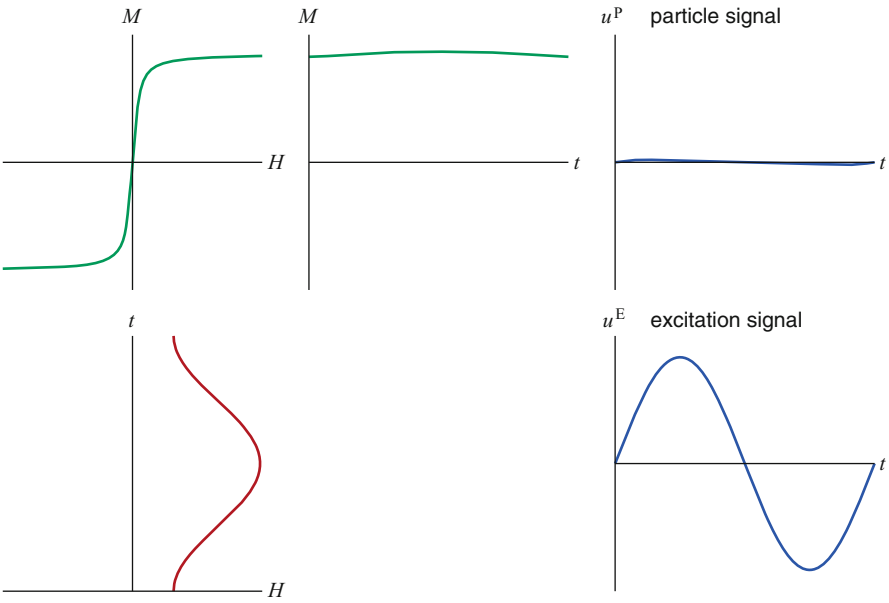

Fig. 2.19 Particle response to a sinusoidal magnetic field with high offset. Due to the offset, the particle magnetization stays in saturation over the complete scan-time. Hence, no signal is induced in the receive coil

2.4.2 Sampling of Volumes

By moving either the object or the FFP in space, different voxels in space can be selected. In this way, the complete volume of interest can be examined by measuring the amount of higher harmonics at each sampling position. This single-voxel MPI acquisition method is schematically illustrated in Fig. 2.20. The movement of either the object or the FFP can easily be realized in 3D, which allows to construct a simple 3D MPI scanner. The first publication on MPI shows 2D images that have been acquired this way [GW05], while in the work of Goodwill et al., first 3D images acquired in this single-voxel manner have been published [GSSC09]. The largest disadvantage of the single-voxel MPI method is its slowness, which is due to the fact that at each sampling position, a complete MPI measurement – lasting at least the repetition time T^R – has to be performed. In practice, due to the limited excitation field amplitude, one has to average the signal over several repetitions to gain an adequate SNR. This either results in measurement times of several minutes for samples of very limited size or in very coarse spatial sampling of the object. Therefore, the single-voxel MPI protocol will never be sufficient to perform in vivo measurements with satisfying spatial and temporal resolution. This is especially true for living specimen or structures of interest, which move rather fast, e.g., vessels in the cardiovascular system.

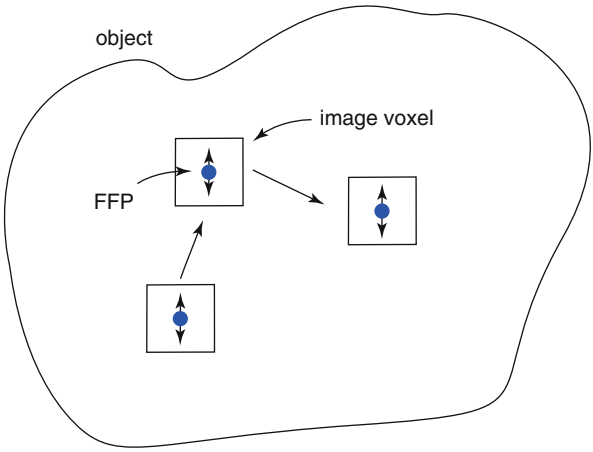

Fig. 2.20 Sampling an image volume using the single-voxel method. The FFP is moved to each position at which the particle distribution is to be imaged. After each positioning, the excitation field is applied and the spectral components stemming from particles in the close vicinity of the FFP are recorded using the receive coil

2.4.3 Properties of the Selection Field

As can be observed in Fig. 2.18, the gradient strength of the selection field varies in different directions. More precisely, the gradient strength in y-direction $G_y := \frac{\partial H_y}{\partial y}$ is twice the value of that in x-direction $G_x := \frac{\partial H_x}{\partial x}$ but has a different sign. If one would look at the field within the yz-plane, one would find that the gradient in z-direction $G_z := \frac{\partial H_z}{\partial z}$ has the same value as the gradient in x-direction. Hence, the relation between the three gradient strengths is given by

$$G_y = -2G_x = -2G_z. \tag{2.52}$$

This asymmetry is not a coincidence but due to the very nature of the Maxwell equations (see Appendix A). Gauß's law of magnetism states that the divergence of the magnetic field, which is the sum of the spatial derivatives in x-, y- and z-directions, has to be zero, i.e.,

$$\nabla \cdot \boldsymbol{H} = \frac{\partial H_x}{\partial x} + \frac{\partial H_y}{\partial y} + \frac{\partial H_z}{\partial z} = 0. \tag{2.53}$$

One way to fulfill this relation is to chose the gradients in the way outlined in (2.52). Certainly, Maxwell's equations allow other field shapes such as

$$G_y = -G_x \quad \text{and} \quad G_z = 0, \tag{2.54}$$

which generates a field-free line along the z-direction (see Sect. 6.3). What is, however, not possible is that the gradient strength along the three principle axes have the same absolute value. This asymmetry of the selection field has impact on the spatial resolution of MPI, which is in y-direction twice as high as in x- and z-directions.

2.4.3.1 Gradient Matrix

Using the observations outlined above, the selection field shown in Fig. 2.19 can be written as

$$\boldsymbol{H}^{\mathrm{S}}(\boldsymbol{r}) = \begin{pmatrix} G_x & 0 & 0 \\ 0 & G_y & 0 \\ 0 & 0 & G_z \end{pmatrix} \boldsymbol{r} = G \begin{pmatrix} -\frac{1}{2} & 0 & 0 \\ 0 & 1 & 0 \\ 0 & 0 & -\frac{1}{2} \end{pmatrix} \boldsymbol{r}. \tag{2.55}$$

where $G = G_y$ is the steepest gradient of the field. By defining the gradient matrix

$$\boldsymbol{G} := \begin{pmatrix} G_x & 0 & 0 \\ 0 & G_y & 0 \\ 0 & 0 & G_z \end{pmatrix}, \tag{2.56}$$

the selection field can be compactly written as

$$\boldsymbol{H}^{\mathrm{S}}(\boldsymbol{r}) = \boldsymbol{G}\boldsymbol{r}. \tag{2.57}$$

Note that the matrix $\boldsymbol{G}$ is the Jacobian matrix or vector gradient of the vectorial function $\boldsymbol{H}^{\mathrm{S}}(\boldsymbol{r})$.

In order for the area around the FFP where the particles are unsaturated to be sufficiently small, the gradient strength G, measured in units of $\mathrm{Tm}^{-1}\mu_0^{-1}$, has to be sufficiently high. For small scanner devices gradient strengths of more than $10\,\mathrm{Tm}^{-1}\mu_0^{-1}$ are feasible. For a human scanner, the highest feasible gradient strength is about $3\,\mathrm{Tm}^{-1}\mu_0^{-1}$ for a system realized by resistive coils or permanent magnets, while superconductors would allow for up to $6\,\mathrm{Tm}^{-1}\mu_0^{-1}$ gradient strength.

2.5 Performance Upgrade: Drive Field

The basic MPI setup described in the last section relies on the movement of the sample in relation to the FFP, while the MPI signal is generated by an excitation field. This results in a very slow image acquisition. Furthermore, as the excitation field is limited in amplitude to ensure that the FFP stays within a voxel at each measurement, the method is not optimal regarding the SNR of the measurement signal. In this section, an improved MPI acquisition method is introduced, which substantially shortens the acquisition time enabling real-time MPI as has been experimentally proven in [GWB08] and [WGR+09].

2.5.1 Moving the Field-Free Point

In order to speed up the imaging process, one just has to break the rule that the FFP has to stay within an image voxel during one measurement. Instead, by increasing

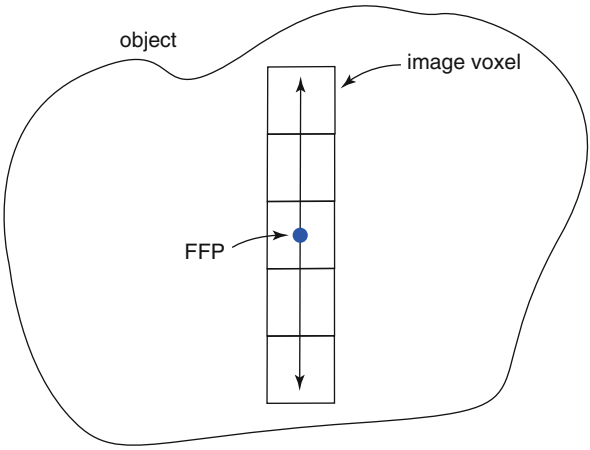

Fig. 2.21 Sampling a volume using the drive-field method. Using an excitation field of high amplitude, the FFP is rapidly moved back and forth along a line, which covers several image voxels. As the particle response depends on the position on the line, the particle concentration can be recovered by reconstruction

the excitation field amplitude, the FFP is moved back and forth along a line in direction of the field vector of the excitation field. As can be seen in Fig. 2.21, during one measurement one receives respective signals not only from the particles of one voxel but from the particles of several voxels along the FFP trajectory. Instead of moving the FFP *in between* measurements, the FFP is now moved *during* the measurement. This leads to a significant increase of the temporal resolution of the method substantiated by the following facts:

- The sample need not to be moved between measurements. This drastically improves the latency of the method.
- The acquisition time of a single measurement is not increased. The repetition time of one measurement is still $T^{\mathrm{R}} = \frac{1}{f^{\mathrm{E}}}$.
- Instead of several measurements at different positions, one now needs only a single measurement to sample a complete line.

The performance improvement is thus at least in the order of the number of voxels along the line covered by the FFP movement. Due to this huge improvement, the use of a drive field has been proposed and used in measurements already in the first MPI publication [GW05].

2.5.2 How to Move the Field-Free Point Nonmechanically

To realize a nonmechanical movement of the FFP, one needs to superimpose a magnetic field on top of the selection field. This magnetic field should ideally be homogeneous in space such that the gradient strength of the total field is not changed.

The homogeneous field is usually called the drive field due to its role of driving the FFP through the space. To move the FFP to position $\boldsymbol{r}^{\mathrm{FFP}}$, the magnetic field at

this very position has to be canceled out. The superposition of the selection field $\boldsymbol{H}^{\mathrm{S}}$ and the drive field $\boldsymbol{H}^{\mathrm{D}}$ thus has to fulfill

$$\boldsymbol{H}\left(\boldsymbol{r}^{\mathrm{FFP}}\right) = \boldsymbol{H}^{\mathrm{S}}\left(\boldsymbol{r}^{\mathrm{FFP}}\right) + \boldsymbol{H}^{\mathrm{D}} = \boldsymbol{0}. \tag{2.58}$$

Hence, to move the FFP to position $\boldsymbol{r}^{\mathrm{FFP}}$, the drive field has to be chosen as

$$\boldsymbol{H}^{\mathrm{D}} = -\boldsymbol{H}^{\mathrm{S}}\left(\boldsymbol{r}^{\mathrm{FFP}}\right) = -\boldsymbol{G}\boldsymbol{r}^{\mathrm{FFP}}. \tag{2.59}$$

To determine the position of the FFP for the given drive field $\boldsymbol{H}^{\mathrm{D}}$ one can solve for $\boldsymbol{r}^{\mathrm{FFP}}$ yielding

$$\boldsymbol{r}^{\mathrm{FFP}} = -\boldsymbol{G}^{-1}\boldsymbol{H}^{\mathrm{D}}. \tag{2.60}$$

The inverse of the gradient matrix is given by

$$\boldsymbol{G}^{-1} = \begin{pmatrix} \frac{1}{G_x} & 0 & 0 \\ 0 & \frac{1}{G_y} & 0 \\ 0 & 0 & \frac{1}{G_z} \end{pmatrix}. \tag{2.61}$$

Hence, the change of the drive field linearly translates to a movement of the FFP. In Fig. 2.22, it is illustrated how the superposition of the drive field translates the FFP in 1D, while in Fig. 2.23 a 2D FFP translation is shown.

2.5.3 Drive-Field Waveform

Now that we know how to adjust the drive field to move the FFP to a certain position, we have to chose how the field strength changes temporarily to cover a certain FOV. For now an 1D FOV is considered.

When choosing the drive-field waveform, one has to keep in mind that a change of the magnetic field induces a voltage in the receive coil, which masks the induced particle signal. As introduced in Sect. 2.5.1, the drive field is actually the excitation field with a high amplitude. Hence, the same method can be applied to distinguish between the induced particle signal from the induced drive-field signal. As it has been discussed in Sect. 2.3.3, the excitation field and in turn the drive field should have a sinusoidal temporal progression, so that the masking of the excitation signal is limited to the excitation frequency, while all higher harmonics of the particle signal can be easily detected.

For a sinusoidal drive field directed in x-direction

$$\boldsymbol{H}^{\mathrm{D}}(t) = -A_x^{\mathrm{D}} \cos\left(2\pi f^{\mathrm{E}} t\right) \boldsymbol{e}_x, \tag{2.62}$$

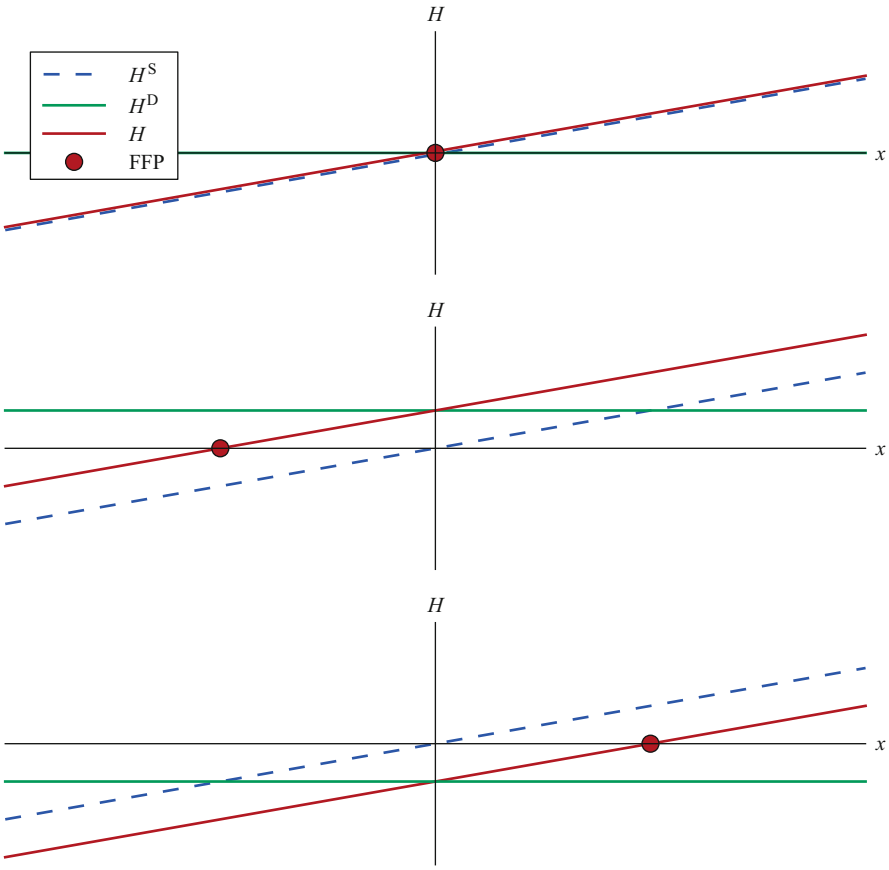

Fig. 2.22 1D translation of the FFP achieved by the superposition of a homogeneous drive field pointing in the opposite direction of the translation

the total magnetic field in x-direction at time t is given by

$$H_x(x,t) = -A_x^{\mathrm{D}} \cos\left(2\pi f^{\mathrm{E}} t\right) + G_x x. \tag{2.63}$$

The FFP, which satisfies $H_x(x,t) = 0$, is thus located at position

$$x^{\mathrm{FFP}}(t) = \frac{A_x^{\mathrm{D}}}{G_x} \cos\left(2\pi f^{\mathrm{E}} t\right). \tag{2.64}$$

Hence, the FFP oscillates on the x-axis along a line within the interval

$$\left[-\frac{A_x^{\mathrm{D}}}{G_x}, \frac{A_x^{\mathrm{D}}}{G_x}\right]. \tag{2.65}$$

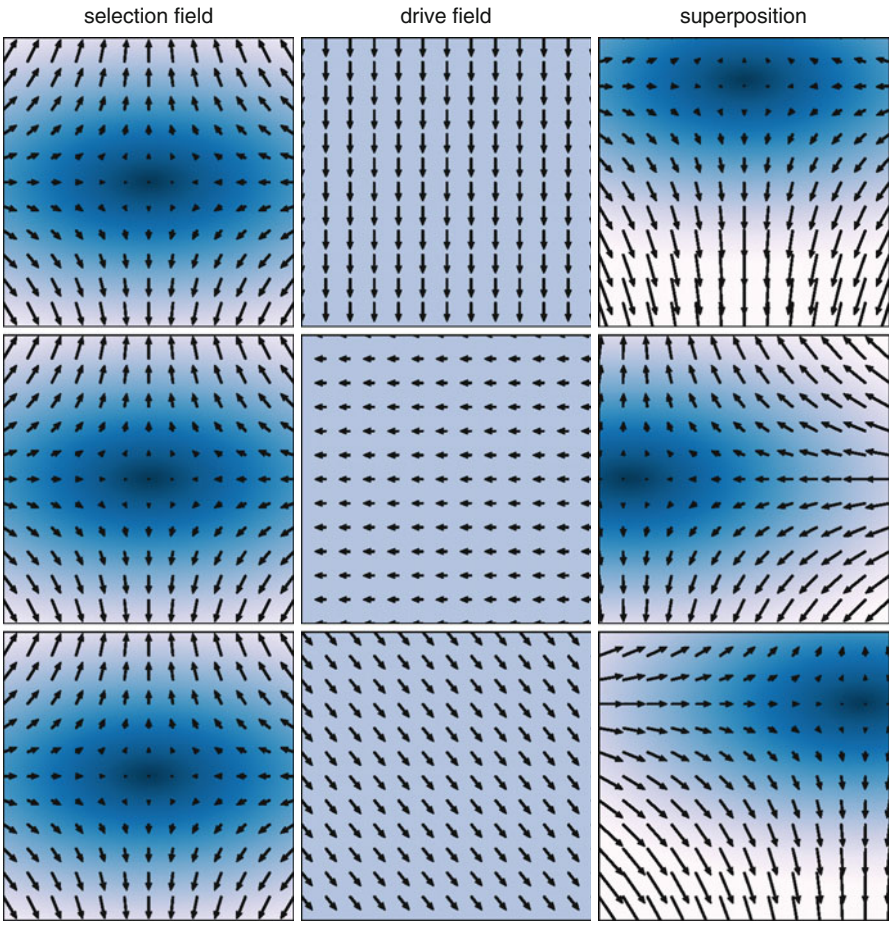

Fig. 2.23 2D translation of the FFP achieved by the superposition of a homogeneous drive field

The FFP has its highest speed at the center and its lowest speed at the edges of the FOV. This has impact on the image quality, which can be slightly higher in the center.

2.5.4 Individual Signals

In contrast to the mechanical way of spatial encoding, the drive field method yields a measurement signal containing contributions of particles at different positions. One obvious question is whether it is possible to separate the individual signals of particles located at different positions.

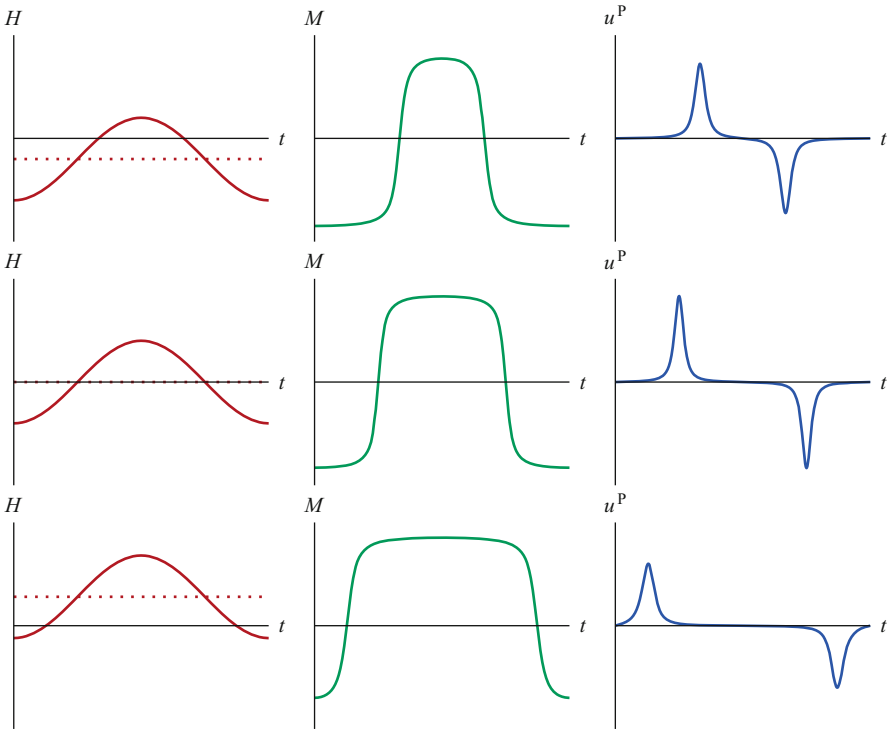

Fig. 2.24 Effect of applying a constant offset to the sinusoidal drive field. As can be seen, the locations of the peaks in the induced particle signal are shifted by the applied offset

Without the selection field all particles in space behave the same as the drive field is homogeneous in space. By applying the selection field, a spatially dependent offset is superimposed onto the drive field. Consequently, the time at which the total field crosses zero is shifted by the offset such that the zero-crossings at two different positions happen at different time points. This conclusion has already been formulated in (2.64), which implies that the FFP (zero-crossing of the gradient field) is unique in space during the complete scanning period.

Now recall that the induced particle signal is maximum when the magnetization flips its direction. When moving the FFP through the FOV, the particle magnetization flips only at a single position in space, which is the FFP. Hence, at time t, the highest contribution to the induced signal is of particles located at position $x^{\mathrm{FFP}}(t)$. In Fig. 2.24, the signals induced by a small object located at different positions are shown. As can be seen, each signal contains one positive and one negative peak and has a rotational symmetry. This is due to the symmetry of the sinusoidal excitation function and the derivative applied to the particle magnetization. The two time points at which the peaks occur are shifted according to the object position x^{delta}

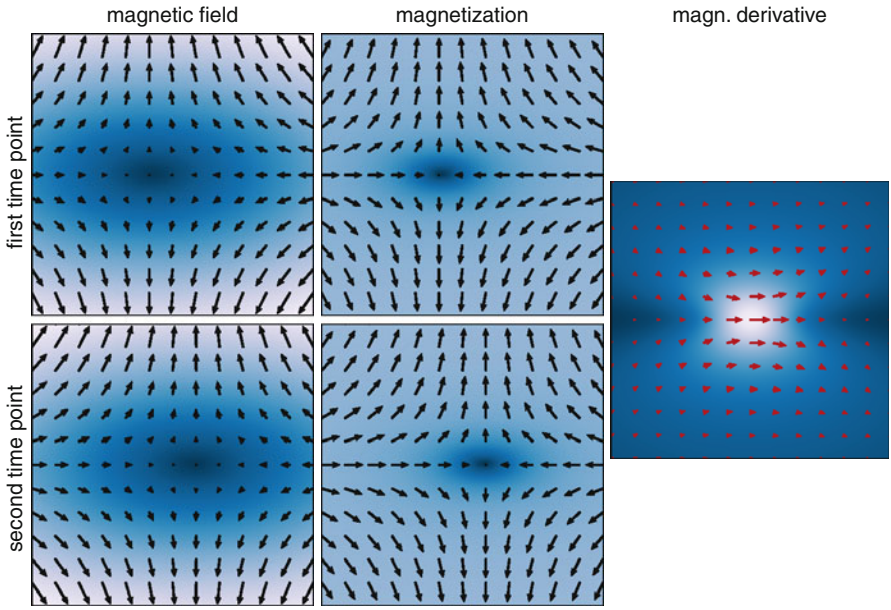

Fig. 2.25 FFP moving from the left to the right in x-direction acting as a sensitiv spot on the particle distribution. On the *left*, the FFP field is shown at two subsequent time points. In the *middle*, the particle magnetization of a homogeneous particle distribution is illustrated at both time points. On the *right*, the time derivative of the magnetization is shown. For better illustration, the interval between the considered time points is finite, whereas for the calculation of the derivative an infinitisimal small time interval is used

and can be computed by

$$t_1 = \frac{1}{2\pi f^{\mathrm{E}}} \arccos\left(\frac{G_x}{A_x^{\mathrm{D}}} x^{\mathrm{delta}}\right), \tag{2.66}$$

$$t_2 = T^{\mathrm{R}} - \frac{1}{2\pi f^{\mathrm{E}}} \arccos\left(\frac{G_x}{A_x^{\mathrm{D}}} x^{\mathrm{delta}}\right). \tag{2.67}$$

The peaks have a finite width even for infinitesimal small objects. This is due to the finite steepness of the magnetization curve, which induces this blurring. The height of the peaks varies with the position x^{delta} and is maximum at the origin. Going to the edges of the FOV, the height decreases. In fact, the envelope of the signals at different positions resembles the sinusoidal excitation pattern. This variation in the signal intensity is induced by the speed of the FFP, which is slow at the edges and maximum at the origin. The time derivative in (2.36) is responsible for this dependency of the signal intensity on speed of the field change. A mathematical explanation for the sinusoidal envelope is given in the next section.

In Fig. 2.25, the signal contribution of different particles in space is illustrated when the FFP moves along a certain direction (here, the x-direction). This intensity

map can be seen as the sensitivity around the FFP. When sweeping the FFP through the space, the sensitive spot in the center of the sensitivity map directly follows the FFP. What is not directly obvious is that the FFP sensitivity map seems to be wider in the orthogonal direction to the FFP movement, although the FFP gradient is, in the considered case, by a factor of 2 smaller in x-direction than in y-direction. The reason for this is that in orthogonal direction to the FFP movement even the saturated particles rotate and therefore change their magnetization.

In summary, the spatially dependent selection field leads to a time shift in the particle response, which gives each position in space a unique profile of the voltage being induced in the receive coil. Thus, it is possible to compute the particle distribution given the known signal profiles for all positions in the FOV.

2.5.5 Convolution with the FFP Kernel

As we have seen in the last section, the signals induced by different particles in space are shifted according to their position. Hence, the question arises, whether the imaging equation can be mathematically described by a convolution, which is a property of linear shift-invariant systems. As it is shown next, for 1D imaging the system can indeed be formulated as a convolution.

2.5.5.1 Convolution in Time Space

Assuming a homogeneous receive coil sensitivity, which pics up the x-component of the magnetization, i.e., $\boldsymbol{p}^{\mathrm{R}} = (p^{\mathrm{R}}, 0, 0)^{\mathsf{T}}$, the induced voltage can be written in the form

$$u^{\mathrm{P}}(t) = -\mu_0 p^{\mathrm{R}} \int_{-\infty}^{\infty} \frac{\partial M(x,t)}{\partial t}\,\mathrm{d}x, \tag{2.68}$$

see (2.36). Here, $M(x,t)$ is the x-component of the particle magnetization, which can be expressed as $M(x,t) = c(x)\overline{m}(x,t)$ (see (2.17)). Assuming Langevin particles, for which the magnetic moment can be written as a function of the applied field, the induced voltage can be expressed as

$$u^{\mathrm{P}}(t) = -\mu_0 p^{\mathrm{R}} \int_{-\infty}^{\infty} c(x) \frac{\partial \overline{m}'(H(x,t))}{\partial t}\,\mathrm{d}x. \tag{2.69}$$

By exploiting the chain rule

$$\frac{\partial \overline{m}'(H(x,t))}{\partial t} = \frac{\partial \overline{m}(H(x,t))}{\partial H} \frac{\partial H(x,t)}{\partial t} \tag{2.70}$$

one derives

$$u^{\mathrm{P}}(t) = -\mu_0 p^{\mathrm{R}} \int_{-\infty}^{\infty} c(x)\overline{m}'(H(x,t)) \frac{\partial H(x,t)}{\partial t}\,\mathrm{d}x. \tag{2.71}$$

where $\overline{m}'(H) = \frac{\partial \overline{m}(H)}{\partial H}$ is the derivative of the mean magnetic moment. The shape of the derivative has already been discussed in Sect. 2.2.3. Inserting the total magnetic field $H(x,t) = H^{\mathrm{D}}(t) + G_x x$ yields

$$u^{\mathrm{P}}(t) = -\mu_0 p^{\mathrm{R}} (H^{\mathrm{D}})'(t) \int_{-\infty}^{\infty} c(x) \overline{m}'(H^{\mathrm{D}}(t) + G_x x)\, \mathrm{d}x. \tag{2.72}$$

By defining the kernel

$$\tilde{m}(x) := -\mu_0 p^{\mathrm{R}} \overline{m}'(G_x x) \tag{2.73}$$

and using the reflectional symmetry $\tilde{m}(x) = \tilde{m}(-x)$ one derives

$$u^{\mathrm{P}}(t) = (H^{\mathrm{D}})'(t) \int_{-\infty}^{\infty} c(x) \tilde{m}(-G_x^{-1} H^{\mathrm{D}}(t) - x)\, \mathrm{d}x, \tag{2.74}$$

which can be written as a convolution:

Theorem 2.1. *For a 1D imaging sequence, the relation between the particle concentration c and the induced voltage u^P can be described as*

$$u^P(t) = (H^D)'(t)\, (c * \tilde{m}) \left(-G_x^{-1} H^D(t)\right), \tag{2.75}$$

which consists of a convolution weighted with the time derivative of the drive field.

One can identify in (2.75) that the convolved particle distribution is weighted with the factor $(H^{\mathrm{D}})'(t)$, which is the change of the magnetic drive field that is proportional to the speed of the FFP. As the FFP speed is slow at the edges and fast at the center of the FOV, it is clear that the signal amplitude is damped at the edges of the FOV (see Fig. 2.24).

2.5.5.2 FFP Speed Normalization

By dividing the signal through the derivative of the excitation function

$$u^{\mathrm{N}}(t) := \frac{u^{\mathrm{P}}(t)}{(H^{\mathrm{D}})'(t)} = (c * \tilde{m}) \left(-G_x^{-1} H^{\mathrm{D}}(t)\right), \tag{2.76}$$

the signal is compensated for the varying speed of the FFP movement. Here, one has to drop the signal at those time points where $(H^{\mathrm{D}})'(t) = 0$, which is the case when the FFP reaches the edges of the FOV and, therefore, no signal is induced in the receive coil. In the following, the signal is neglected at these time points.

2.5.5.3 Gridding on Spatial Interval

For equidistantly sampled time points, the convolution on the right-hand side of (2.76) is evaluated at non-equidistant values. By applying the coordinate transform

$$x^{\mathrm{FFP}}(t) = -\frac{H^{\mathrm{D}}(t)}{G_x} = \frac{A_x^{\mathrm{D}}}{G_x}\cos(2\pi f^{\mathrm{E}} t), \tag{2.77}$$

the time signal can be mapped onto a spatial interval and described by an ordinary convolution:

Theorem 2.2. *By normalizing the induced signal for the FFP speed (2.76) and applying the coordinate transform (2.77), the relation between the particle concentration c and the transformed signal u^x can be described as*

$$u^x(x^{FFP}) = u^N\left(\frac{1}{2\pi f^E}\arccos\left(\frac{G_x}{A_x^D}x^{FFP}\right)\right) = (c * \tilde{m})\,(x^{FFP}), \tag{2.78}$$

which consists of an ordinary convolution.

It should be noted that only the first half of the time interval $[0, T^{\mathrm{R}})$ is used in (2.78). This is due to the fact that the mapping between the time and the FFP is not bijective when considering the complete time period $[0, T^{\mathrm{R}})$. However, in the first half of the this interval, i.e., for one sweep of the FFP through the FOV, the mapping is bijective.

2.5.6 2D/3D Imaging

Until now, only 1D movement of the FFP has been considered. By applying a sinusoidal field excitation along a certain direction, the FFP moves along a line. The path of the FFP represents the sampling trajectory in MPI. In order to image a volume, the FFP has to be steered along a 3D trajectory. In contrast to 1D imaging, where the path of the FFP movement is fixed to be a line, in 3D one has the freedom to use several different trajectories to sample the volume of interest. Let the desired imaging volume be a cuboid

$$\Omega := \left[-\frac{l_x}{2}, \frac{l_x}{2}\right] \times \left[-\frac{l_y}{2}, \frac{l_y}{2}\right] \times \left[-\frac{l_z}{2}, \frac{l_z}{2}\right], \tag{2.79}$$

where l_x, l_y, and l_z are the side lengths. The path

$$\boldsymbol{\psi}(t) = \begin{pmatrix} \psi_x(t) \\ \psi_y(t) \\ \psi_z(t) \end{pmatrix}, \tag{2.80}$$

along which the FFP travels can be implicitly defined as

$$\boldsymbol{H}(\boldsymbol{\psi}(t), t) = \mathbf{0}, \quad t \in [0, T^{\mathrm{R}}). \tag{2.81}$$

For ideal magnetic fields, i.e., a linear selection field and a homogeneous drive field, the trajectory can be explicitly expressed as

$$\boldsymbol{\psi}(t) = -\boldsymbol{G}^{-1}\boldsymbol{H}^{\mathrm{D}}(t), \tag{2.82}$$

see (2.60). Hence, there is a direct linear dependency between the drive field and the FFP position. To move the FFP at arbitrary positions in 3D space, the drive field, thus needs to be freely adjustable. This can be accomplished by using the superposition of three homogeneous drive fields, which are orientated along the three main axes of the coordinate system, i.e.,

$$\begin{aligned}
\boldsymbol{H}_x^{\mathrm{D}}(t) &= H_x^{\mathrm{D}}(t)\boldsymbol{e}_x, \\
\boldsymbol{H}_y^{\mathrm{D}}(t) &= H_y^{\mathrm{D}}(t)\boldsymbol{e}_y, \\
\boldsymbol{H}_z^{\mathrm{D}}(t) &= H_z^{\mathrm{D}}(t)\boldsymbol{e}_z.
\end{aligned} \tag{2.83}$$

In practice, the fields are generated by three different coil units, which are driven by independent currents $I_x^{\mathrm{D}}(t)$, $I_y^{\mathrm{D}}(t)$, and $I_z^{\mathrm{D}}(t)$. The magnetic drive fields are then given by

$$\begin{aligned}
\boldsymbol{H}_x^{\mathrm{D}}(t) &= I_x^{\mathrm{D}}(t)p_x^{\mathrm{D}}\boldsymbol{e}_x, \\
\boldsymbol{H}_y^{\mathrm{D}}(t) &= I_y^{\mathrm{D}}(t)p_y^{\mathrm{D}}\boldsymbol{e}_y, \\
\boldsymbol{H}_z^{\mathrm{D}}(t) &= I_z^{\mathrm{D}}(t)p_z^{\mathrm{D}}\boldsymbol{e}_z,
\end{aligned} \tag{2.84}$$

where p_x^{D}, p_y^{D}, and p_z^{D} denote the sensitivities of the three drive-field coil units. The superposition of the three drive fields leads to

$$\boldsymbol{H}^{\mathrm{D}}(t) = \boldsymbol{H}_x^{\mathrm{D}}(t) + \boldsymbol{H}_y^{\mathrm{D}}(t) + \boldsymbol{H}_z^{\mathrm{D}}(t) = \begin{pmatrix} I_x^{\mathrm{D}}(t)p_x^{\mathrm{D}} \\ I_y^{\mathrm{D}}(t)p_y^{\mathrm{D}} \\ I_z^{\mathrm{D}}(t)p_z^{\mathrm{D}} \end{pmatrix}. \tag{2.85}$$

Hence, the field vector of the total drive field indeed can be adjusted in any direction in space when superimposing three orthogonal drive fields. Inserting (2.85) in (2.82) yields the FFP position at time t:

$$\begin{aligned}
\psi_x(t) &= -\frac{1}{G_x} I_x^{\mathrm{D}}(t)p_x^{\mathrm{D}}, \\
\psi_y(t) &= -\frac{1}{G_y} I_y^{\mathrm{D}}(t)p_y^{\mathrm{D}}, \\
\psi_z(t) &= -\frac{1}{G_z} I_z^{\mathrm{D}}(t)p_z^{\mathrm{D}}.
\end{aligned} \tag{2.86}$$

Hence, by varying the currents in the three drive-field coil units, the FFP is moved in space with a linear dependency on the drive-field current. The currents are maximum when moving the FFP to corners of the FOV Ω. For instance, to move the FFP to the FOV corner $\left(\frac{l_x}{2}, \frac{l_y}{2}, \frac{l_z}{2}\right)^\mathsf{T}$, the currents have to be set to

$$I_x^\mathrm{D} = -\frac{G_x l_x}{p_x^\mathrm{D}}, \quad I_y^\mathrm{D} = -\frac{G_y l_y}{p_y^\mathrm{D}}, \quad I_z^\mathrm{D} = -\frac{G_z l_z}{p_z^\mathrm{D}}.$$

If the selection field has its highest gradient strength in y-direction, i.e., $G_y = -\frac{G_x}{2} = -\frac{G_z}{2}$ and if the side lengths of the FOV are equal, i.e., if the FOV is a cube, the currents in the x- and z-directions will be by a factor of 2 smaller than in the y-direction. In practice, the currents are chosen to be as high as possible to increase the SNR of the measurement signal yielding a cuboid with one short and two long axes, i.e.,

$$l_y = \frac{l_x}{2} = \frac{l_z}{2}. \tag{2.87}$$

To steer the FFP through the FOV, the current waveform has to be appropriately chosen. In the following sections, the most important MPI trajectories are discussed, namely, the Cartesian trajectory and the Lissajous trajectory. For alternative trajectories, for instance, the spiral and the radial sampling pattern, we refer the reader to [KBS+09].

2.5.6.1 Cartesian Trajectory

Before discussing 3D trajectories, the sampling of a 2D plane is discussed. Without loss of generality, the xy-plane is considered. In this case only the two drive fields in the x- and y-directions are used for moving the FFP. The most obvious choice to sample a rectangular 2D FOV is to use a Cartesian sampling pattern as is shown in Fig. 2.26. This can be accomplished by using sinusoidal currents of different frequency in the two drive-field channels, i.e.,

$$I_x^\mathrm{D}(t) = I_x^0 \sin(2\pi f_x t), \tag{2.88}$$

$$I_y^\mathrm{D}(t) = I_y^0 \sin(2\pi f_y t). \tag{2.89}$$

Here, I_x^0 and I_y^0 are the amplitudes of the drive-field currents. By choosing two frequencies differing substantially in magnitude, i.e.,

$$f_x \gg f_y, \tag{2.90}$$

the FFP rapidly moves back and forth in x-direction, while slowly moving in y-direction. Hence, the FOV is scanned line by line until the complete slice is sampled. The total acquisition time for one sampling period depends on the density

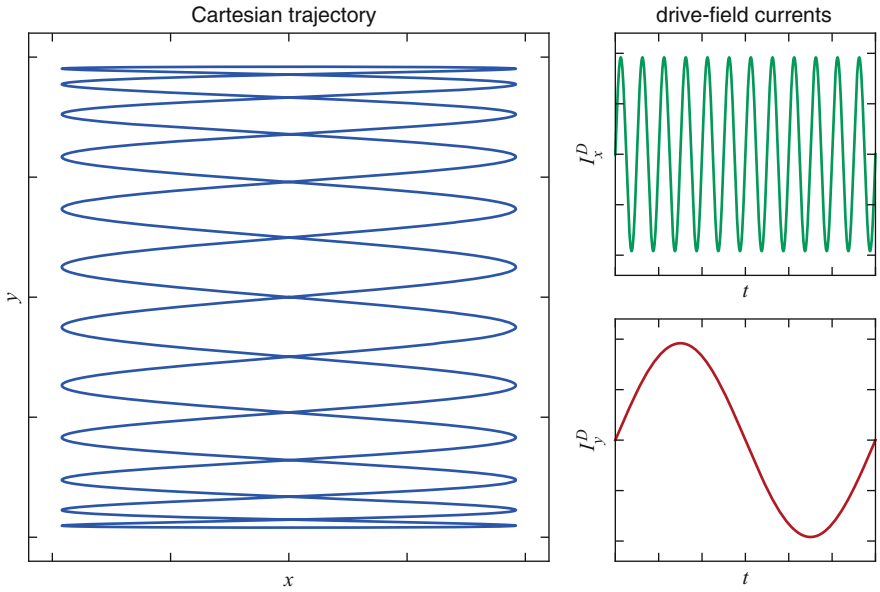

Fig. 2.26 2D Cartesian trajectory generated by sinusoidal currents. The drive-field frequency in x-direction is 12-times higher than the drive-field frequency in y-direction

of the trajectory, which is controlled by the ratio of the excitation frequencies. When using the commensurable frequency ratio

$$\frac{f_y}{f_x} = \frac{1}{N_\mathrm{D}}, \tag{2.91}$$

the repetition time is given by

$$T^\mathrm{R} = \frac{N_\mathrm{D}}{f_x}, \tag{2.92}$$

where N_D is the density parameter. Increasing N_D leads to a higher sampling density with the downside of a longer repetition time.

As the FFP motion is mainly aligned along the x-direction for the Cartesian trajectory, only a single receive coil aligned in x-direction is required. A second orthogonal receive coil aligned in y-direction would only receive a signal of poor SNR. As it has been shown in a simulation study in [KBS+09], the resolution of the Cartesian trajectory is better in the fast direction of the FFP movement than in the slow direction. This is due to the fact that the FFP kernel shown in Fig. 2.25 is wider in the transversal direction of FFP movement than in the direction of FFP movement. One way to mitigate this problem of the Cartesian trajectory is to take two measurements, where the frequencies in the perpendicular coil units are switched in such a way that in each measurement the fast FFP movement is aligned

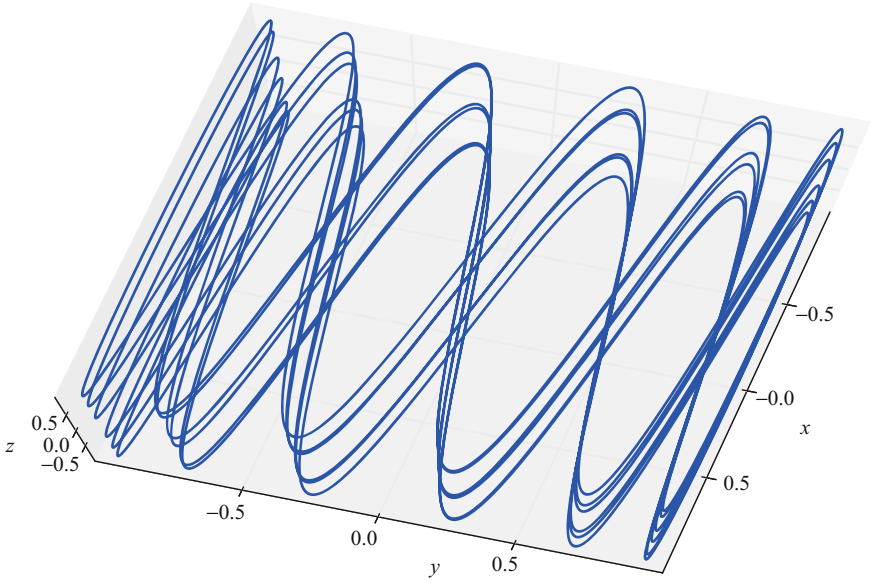

Fig. 2.27 3D Cartesian trajectory generated by three sinusoidal drive-field currents with frequencies $f_x = N_\mathrm{D} f_y = N_\mathrm{D}^2 f_z$ for $N_\mathrm{D} = 6$

along a different direction. Although this can increase the resolution in y-direction, it has the drawback that the sampling density is decreased, when considering a constant acquisition time.

3D Imaging

In order to sample a 3D volume, one has to use also the third drive field

$$I_z^\mathrm{D}(t) = I_z^0 \sin(2\pi f_z t), \tag{2.93}$$

which has a frequency even lower than f_y, i.e.,

$$f_x \gg f_y \gg f_z. \tag{2.94}$$

In this way the volume is scanned slice by slice, where the selection of the slice is done by the drive field orientated in z-direction (see Fig. 2.27). Using

$$f_x = N_\mathrm{D} f_y = N_\mathrm{D}^2 f_z, \tag{2.95}$$

the density of the trajectory can be uniformly changed by adjusting the density parameter N_D. The repetition time is then given by

$$T^\mathrm{R} = \frac{N_\mathrm{D}^2}{f_x}. \tag{2.96}$$

Hence, for 3D imaging an increase of the density by a certain factor increases the repetition time in a squared fashion. Similar to the 2D Cartesian trajectory, it makes sense to change the direction of the fast FFP movement, when measuring the same volume several times.

2.5.6.2 Lissajous Trajectory

Although the Cartesian trajectory is the most obvious sampling scheme to cover a multidimensional FOV, it has not been used in practical implementations so far. Instead, the first 2D [GWB08] and the first 3D [WGR+09] images were obtained using an alternative sampling scheme named Lissajous trajectory.

The Lissajous trajectory also uses sinusoidal currents in each drive-field coil unit (see (2.88) and (2.89)). But instead of using two very different frequencies in the x- and the y-directions, the frequencies are chosen to be similar, i.e.,

$$f_x \approx f_y. \tag{2.97}$$

One way to chose the frequencies in a way that the repetition time T^{R} remains finite is to use commensurable frequencies, which are characterized by the frequency ratios being finite, i.e.,

$$\frac{f_y}{f_x} = \frac{K_x}{K_y}. \tag{2.98}$$

Here, K_x and K_y are natural numbers, which determine the frequency ratio. To obtain similar frequencies, the frequency ratio can be chosen as

$$\frac{f_y}{f_x} = \frac{N_{\mathrm{D}}}{N_{\mathrm{D}}+1}. \tag{2.99}$$

Increasing N_D leads to more similar frequencies and a longer repetition time

$$T^{\mathrm{R}} = \frac{N_{\mathrm{D}}+1}{f_x} = \frac{N_{\mathrm{D}}}{f_y}. \tag{2.100}$$

In Fig. 2.28, an exemplary Lissajous trajectory and the respective current waveforms are illustrated for $N_{\mathrm{D}} = 11$. A segmentation of the 2D Lissajous trajectory into periods of frequency f_x is shown in Fig. 2.29. As can be seen, the FFP travels along ellipsoidal paths and continuously changes the shape of the ellipse. Taking a closer look at the current waveforms by inserting (2.99) into (2.88) and (2.89) leads to

$$I_x^{\mathrm{D}}(t) = I_x^0 \sin(2\pi f_x t), \tag{2.101}$$

$$I_y^{\mathrm{D}}(t) = I_y^0 \sin(2\pi f_x t - \phi(t)), \tag{2.102}$$

where $\phi(t) = \frac{2\pi f_x}{N_{\mathrm{D}}+1} t$ is a time-varying phase drift. Depending on the phase, the FFP travels along a different ellipsoidal path. As for each oscillation with frequency f_x

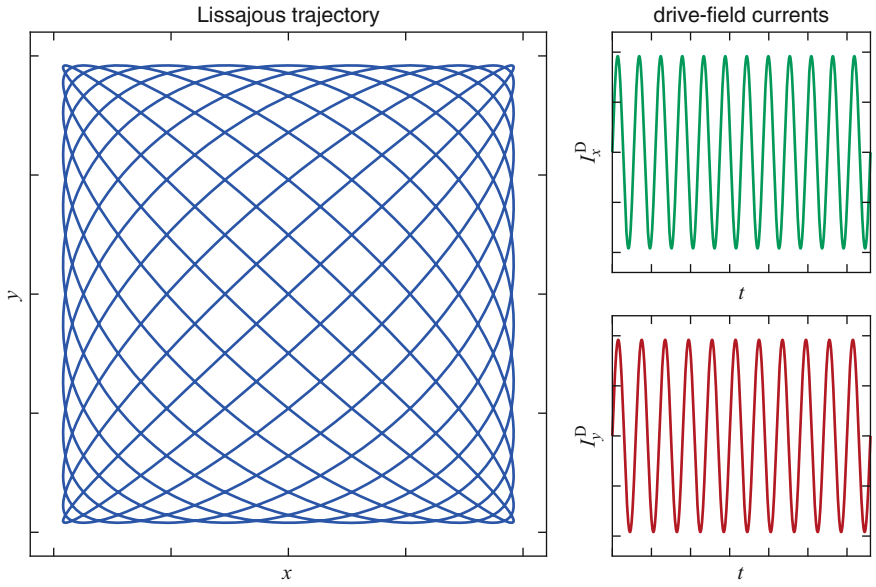

Fig. 2.28 2D Lissajous trajectory generated by sinusoidal drive-field currents. Both excitation frequencies are similar with a frequency ratio of $\frac{11}{12}$

the phase slightly changes (by $\frac{2\pi}{N_D+1}$), the ellipsoidal path is not closed but slightly open. At $t = 0$ and $t = \frac{N_D+1}{2f_x}$, the FFP moves mainly along the bisecting lines. In between these time points, the area covered by the ellipse increases.

3D Imaging

To extend the 2D Lissajous trajectory to 3D, a third sinusoidal excitation is used, which is directed in z-direction. The frequency of this excitation is chosen to be similar to both excitation frequencies in x- and y-directions, i.e.,

$$f_x \approx f_y \approx f_z. \tag{2.103}$$

As for the 2D Lissajous trajectory, the frequencies are chosen to be commensurable to ensure a finite repetition time T^R:

$$\frac{f_y}{f_x} = \frac{K_x}{K_y} \quad \text{and} \quad \frac{f_z}{f_x} = \frac{K_x}{K_z}. \tag{2.104}$$

In this way, the products $f_x K_x$, $f_y K_y$, and $f_z K_z$ equal such that one can define a base frequency

$$f^B = f_x K_x = f_y K_y = f_z K_z, \tag{2.105}$$

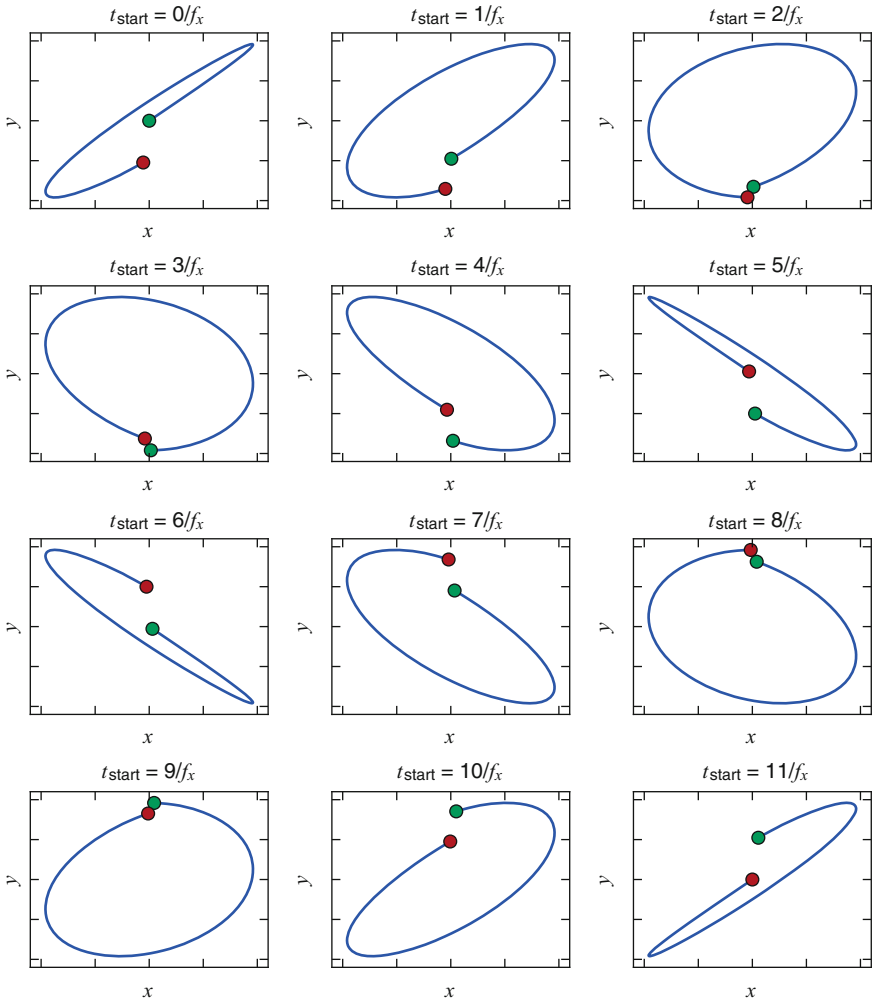

Fig. 2.29 Segmentation of the 2D Lissajous trajectory shown in Fig. 2.28 (frequency ratio $\frac{11}{12}$) into 12 time intervals of time length $\frac{1}{f_x}$. The start time point of each sampling interval is indicated by a *green dot* while the end time point is indicated by a *red dot*

from which the drive-field frequencies can be derived:

$$f_x = \frac{f^{\mathrm{B}}}{K_x}, \quad f_y = \frac{f^{\mathrm{B}}}{K_y}, \quad f_z = \frac{f^{\mathrm{B}}}{K_z}. \tag{2.106}$$

To achieve similar drive-field frequencies, one can use the frequency ratios

$$\frac{f_y}{f_x} = \frac{N_{\mathrm{D}}}{N_{\mathrm{D}}+1} \quad \text{and} \quad \frac{f_z}{f_x} = \frac{N_{\mathrm{D}}}{N_{\mathrm{D}}-1}. \tag{2.107}$$

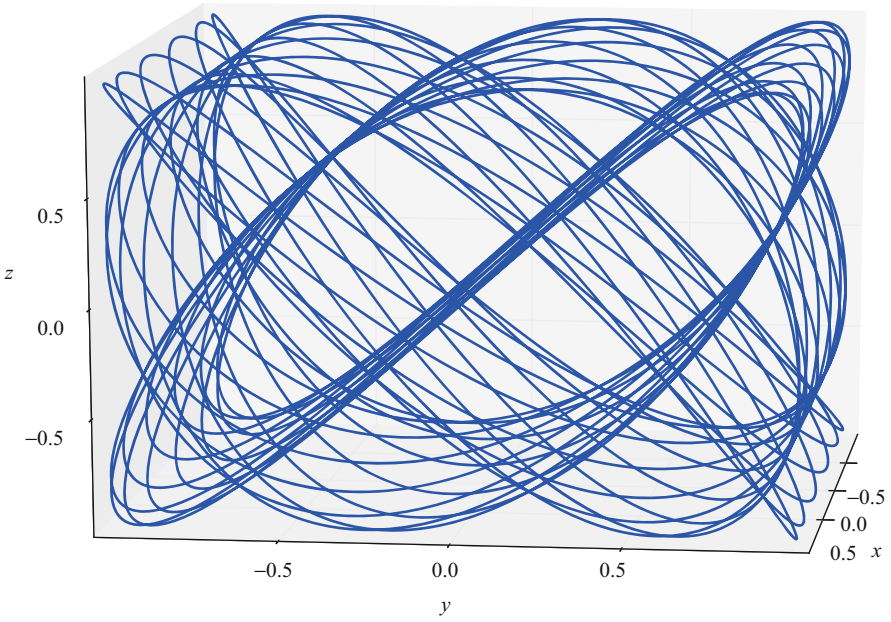

Fig. 2.30 3D Lissajous trajectory generated by three sinusoidal drive-field currents with frequencies $f_x = \frac{N_\mathrm{D}+1}{N_\mathrm{D}} f_y = \frac{N_\mathrm{D}-1}{N_\mathrm{D}} f_z$ for $N_\mathrm{D} = 6$

The repetition time is then given by

$$T^\mathrm{R} = \frac{(N_\mathrm{D}+1)(N_\mathrm{D}-1)}{f_x}. \tag{2.108}$$

Similar to the 3D Cartesian trajectory, the 3D Lissajous trajectory has a repetition time being about N_D^2 times the period of the excitation frequency f_x.

In Fig. 2.30, an exemplary 3D Lissajous trajectory is illustrated. As for the 2D Lissajous trajectory, the FFP travels along ellipsoidal paths, which are in 3D not restricted to the xy-plane but lay within angulated planes.

2.5.6.3 Density of the Trajectory

Both the Cartesian and the Lissajous trajectory are parameterized by the factor N_D, which determines the density as well as the repetition time of the trajectory. In Fig. 2.31, several 2D Cartesian and 2D Lissajous trajectories are illustrated for different density parameters N_D.

The density of the trajectory influences the achievable spatial resolution of MPI. If the density is too low, the resolution is limited by the largest gap within the trajectory. When the density is increased, the spatial resolution in turn increases. However, at some point further increasing the density has no benefit in terms of spatial resolution, as the resolution is then limited by the steepness of the particles' magnetization curve as well as the gradient strength of the selection field.

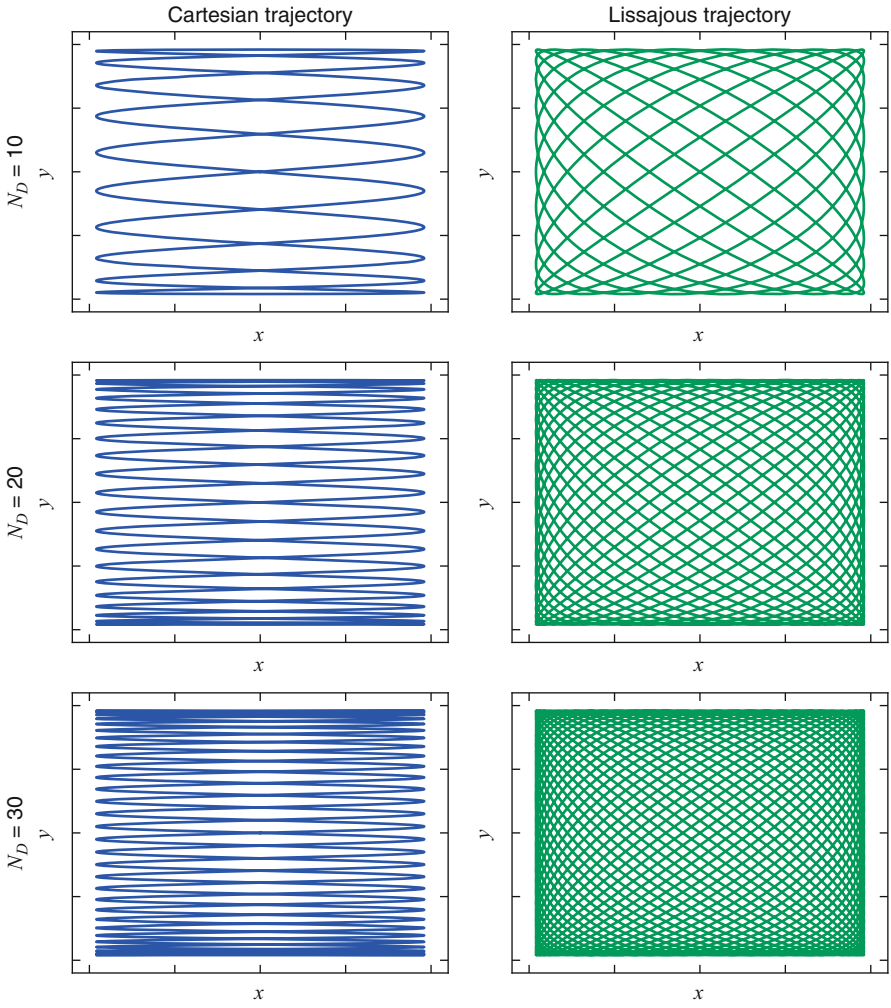

Fig. 2.31 Cartesian and Lissajous trajectories for different density parameters $N_\mathrm{D} \in \{10, 20, 30\}$

2.6 Performance Upgrade: Focus Field

In this section, it is shown that the scanning volume that can be covered by the drive field is limited to few centimeters in length. To overcome this limitation, a method for scanning large scanning volumes is introduced, which utilizes a so-called *focus field*.

2.6.1 Limitations of the Drive Field

By comparing the gradient field strength of the selection field at the FFP and the field strength limit of the drive field as reported in [GW05], one can conclude that the spatial range that is being covered by this electromagnetic FFP movement cannot exceed more than some centimeters. For $20\,\mathrm{mT}\mu_0^{-1}$ drive-field strength and $3\,\mathrm{Tm}^{-1}\mu_0^{-1}$ gradient strength, the FOV is a cuboid with side lengths

$$l_y = 2\frac{A_y^{\mathrm{D}}}{G_y} = 2\frac{20\,\mathrm{mT}\mu_0^{-1}}{3\,\mathrm{Tm}^{-1}\mu_0^{-1}} \approx 13.333\,\mathrm{mm}, \tag{2.109}$$

$$l_x = l_z = 2\frac{A_x^{\mathrm{D}}}{G_x} = 2\frac{20\,\mathrm{mT}\mu_0^{-1}}{1.5\,\mathrm{Tm}^{-1}\mu_0^{-1}} \approx 26.666\,\mathrm{mm}. \tag{2.110}$$

This kind of limitation for the volume of interest is clearly not acceptable for medical applications in general diagnostics, where it is expected to have systems that cover an entire cross section of a human body, as in MRI or CT.

2.6.2 Scanning Large Volumes Using the Focus Field

In order to overcome the limitation to small volumes of interest, one could simply increase the field strength of the drive field. However, while it might be technically feasible to apply fields of several hundred $\mathrm{mT}\mu_0^{-1}$ at frequencies of 25 kHz or even more, it can lead to energy deposition values (SAR) exceeding regulatory limits and to peripheral nerve stimulation (PNS). Consequently, it is not possible to increase the drive-field strength above about $20\,\mathrm{mT}\mu_0^{-1}$ in practice. To still be able to image large FOV, Gleich et al. introduced the focus field in [GWT+10].

For the time being it is sufficient to realize that an increase in amplitude has to be compensated by a decrease in frequency. So, in addition to the drive field, another set of orthogonal, homogeneous fields, called focus fields, are added. For a focus field strength in the dimension of $300\,\mathrm{mT}\mu_0^{-1}$, the coverage of the FOV would be 20 cm for the high gradient direction of a selection field of $3\,\mathrm{Tm}^{-1}\mu_0^{-1}$ and 40 cm for the low gradient directions. The frequency of the focus field, however, is low compared to the drive field, i.e., in the area of a few Hertz such that the field will not be used for imaging alone, which would result in a rather poor performance. Instead, the movement of the FFP will be produced by a combination of the focus and the drive field. This can be done in a multi-station mode, where the focus field is used to move the whole volume that is covered by the drive field, named cuboid or patch, to a certain position within the FOV and keep it there, while the drive field does its job (see Fig. 2.32). This results in covering the volume of interest by cuboids, that constitute small 3D images in their own right, which are then combined into a complete 3D data set.

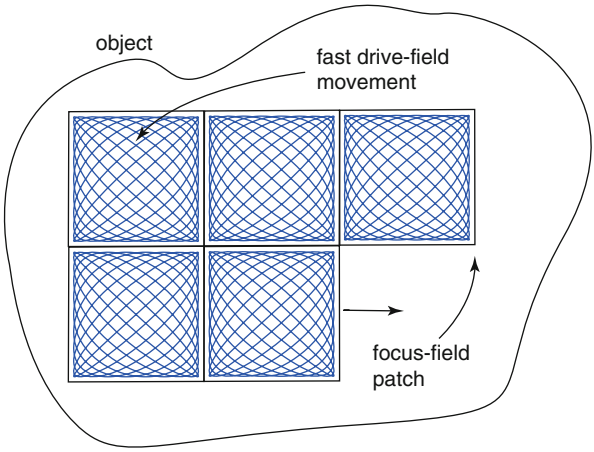

Fig. 2.32 Multi-station approach to sample a large FOV using the combination of the drive field and the focus field. Note that each patch is actually a 3D volume sampled by a 3D Lissajous trajectory

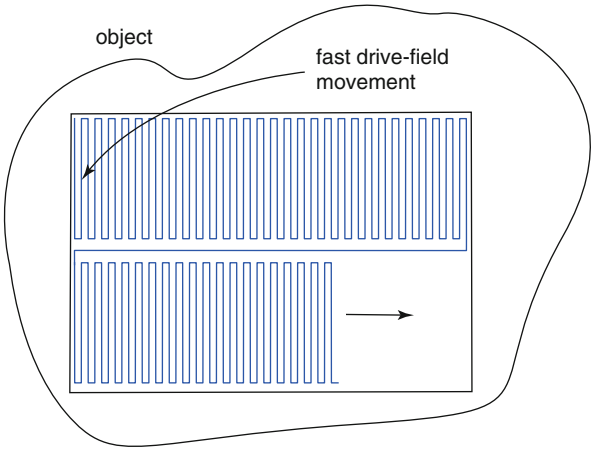

Fig. 2.33 Continuous approach to sample a large FOV using the combination of the drive field and the focus field. Note that each *vertical line* represents a fast 2D Lissajous trajectory with outer normal aligned along the horizontal direction

Another option is to combine a simultaneous variation of both, the focus and the drive field, to produce a continuous movement of the FFP, called continuous mode (see Fig. 2.33). In contrast to the multi-station mode, the resulting image is rather one complete image that covers the volume of interest than a combination of small cuboids.

In addition to just covering the complete volume of interest, the focus field can also be used to realize a different, but very effective imaging mode. If, for example, the area of interest consists of only a sub-volume of the complete FOV, and, moreover, this sub-volume is not rectangular, but rather a part of an irregular 3D shape, then the focus field can be used to image only those cuboids containing the respective sub-volume. The concept of partially sampled FOV by the combination

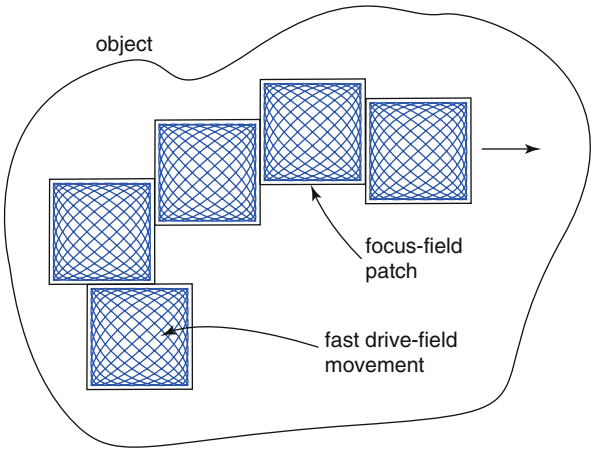

Fig. 2.34 Partial sampling of a large FOV using the combination of the drive field and the focus field

of the drive and the focus field is illustrated in Fig. 2.34. As a result of this sampling strategy, much less space has to be scanned, leading to an effective image acquisition.

As the focus field is a rather new concept introduced in 2010, only first preliminary results of multi-station measurements have been published [SRG+11]. How to reconstruct multi-station focus field data is still an active field of research and, therefore, not discussed in this book.

2.7 Limitations of MPI

In order to discuss potential medical applications of MPI, there is a great interest to asses essential imaging parameters such as the spatial resolution, the temporal resolution, and the sensitivity. Typically, these parameters are linked to each other; for instance, an increase of the sensitivity by averaging the signal comes for the cost of a decrease in temporal resolution.

2.7.1 Spatial Resolution

One of the most important parameters of an imaging method is the spatial resolution. Basically, the spatial resolution describes how close two objects can be to each other such that they can be distinguished. Distinguished means that there is a significant minimum of the gray-value representation in between the two objects. Significant means that the minimum value at the gap is less than half of the maximum value at the objects' positions. Given this definition of spatial resolution, there are several ways to report the resolution, i.e., in lines per millimeter or in line pairs per millimeter. Alternatively, the resolution can be given as a length, which is either

the width in millimeter of the smallest line that can be resolved or the width of the smallest line pair (i.e., the width of the line plus the gap).

In this book, the resolution is given as the size of the smallest line, which can be resolved. This measure has been proposed in the context of MPI in [WBG07] and matches that given by the FWHM of the convolution kernel, which has been used in [RWGB09, GC10].

As the magnetic particle imaging process can in 1D be formulated as a convolution, one can use well-known tools to analyze the spatial resolution [BM03]. In the following, two important resolution measures are discussed: the FWHM resolution and the modulation transfer function (MTF) resolution.

2.7.1.1 Full Width at Half Maximum of the Convolution Kernel

When applying a convolution, sharp structures in a signal are blurred, which leads to a loss of resolution. The actual resolution loss depends on the shape of the convolution kernel. One way to estimate the resolution based on the shape of the convolution kernel is to consider its full width half maximum, which was already introduced in Sect. 2.2.3.

In Fig. 2.35, three different signals resulting from a convolution of line pair phantoms with the MPI convolution kernel $\tilde{m}$ for 1 mm FWHM are shown. As can be seen, the spatial resolution according to the definition outlined above is about 1 mm, which matches the FWHM of the convolution kernel. However, for different kernels both values can differ slightly, for instance for, the Gaussian kernel, which can resolve 0.82 mm structures for 1 mm FWHM.

In Sect. 2.2.3, the FWHM of the derivative of the magnetization characteristic $M'(H)$ was calculated to be $\Delta H^{\text{FWHM}} = 4.16\,\beta^{-1}$. Consequently, the convolution kernel $\tilde{m}$ as defined in (2.73) has an FWHM of

$$R^{\text{FWHM}} = 4.16\frac{1}{\beta G}. \tag{2.111}$$

In Fig. 2.36, the FWHM resolution is plotted versus the gradient strength of the selection field for different particle diameters. As can be seen, the resolution increases inversely proportional with the applied gradient strength. Furthermore, as the factor β depends on the third power of the particle diameter, the resolution increase in a cubic fashion when increasing the particle diameter. In practice, gradient strengths up to $6\,\text{Tm}^{-1}\mu_0^{-1}$ and particle diameters of 30 nm are feasible such that the resolution can potentially be better than 0.5 mm.

While the FWHM criterion is a simple way to analyze the resolution of an imaging system, it is not the most accurate one, as it does not take into account that the resolution can be increased by performing a deconvolution. It further does not consider the SNR of the measured signal. Hence, in practice, the real resolution can be both higher and lower than (2.111) would suggest.

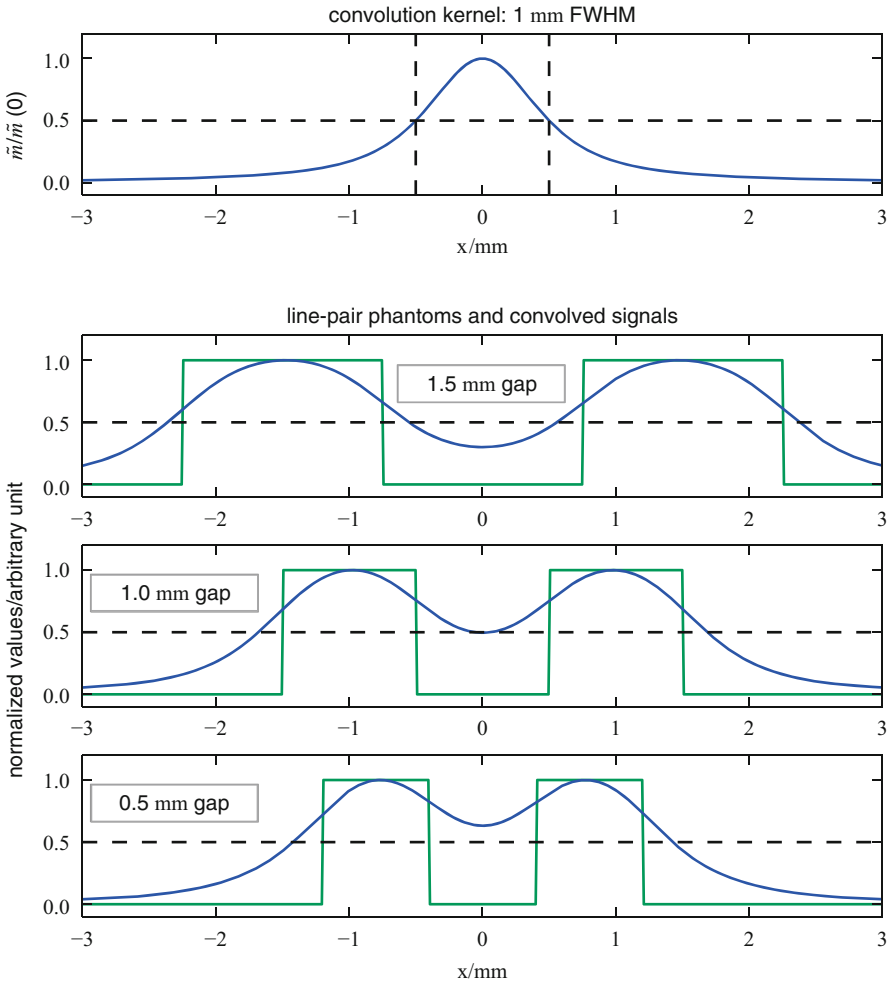

Fig. 2.35 Normalized convolution kernel $\tilde{m}/\tilde{m}(0)$ for 1 mm FWHM (*top*) and normalized convolved signals (*blue*) for several line-pair phantoms consisting of two rectangular dots of the same size and gap (1.5, 1.0, and 0.5 mm). In *green* the original line-pair phantoms are illustrated

2.7.1.2 Modulation Transfer Function

A more sophisticated way to analyze the spatial resolution of an imaging system is to consider the modulation transfer function [Buz08], which allows to relate the spatial resolution to the SNR of the measured signal. The MTF describes how the contrast of an image structure is damped by the convolution of the imaging process. The MTF is a function of the spatial frequency and can be defined in Fourier space where the convolution corresponds to a multiplication of the Fourier transform of the particle concentration

$$\hat{c}(\nu) := \mathcal{F}(c(x)) \tag{2.112}$$

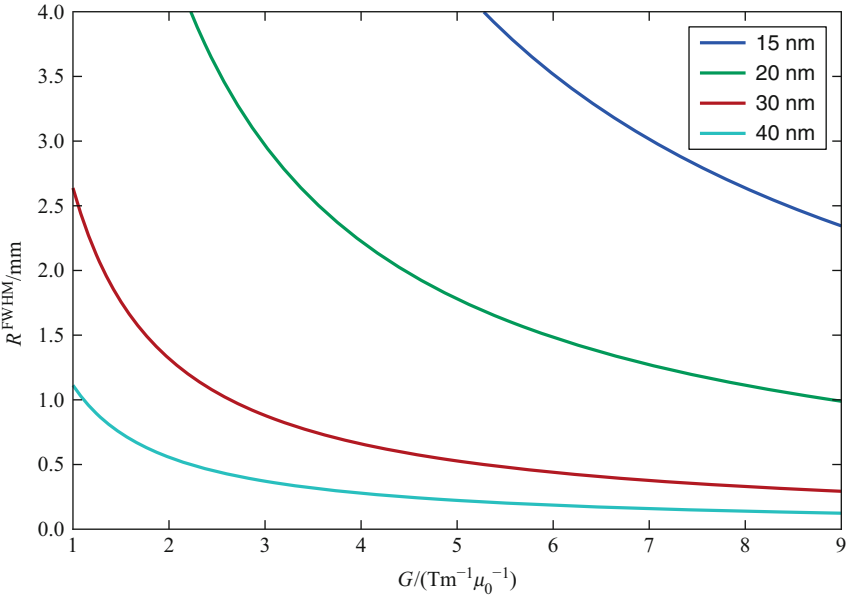

Fig. 2.36 FWHM of the convolution kernel $\tilde{m}$ versus the gradient strength of the selection field for different particle diameters

with the Fourier transform of the convolution kernel

$$\hat{m}(\nu) := \mathcal{F}(\tilde{m}(x)), \tag{2.113}$$

where $\mathcal{F}$ denotes the continuous Fourier transformation. Hence, the Fourier transform of the induced x-space signal $u^x(\tilde{x})$ can be expressed as

$$\hat{u}^x(\nu) := \mathcal{F}(u^x(\tilde{x})) = \hat{c}(\nu)\hat{m}(\nu). \tag{2.114}$$

In (2.114), one can identify the signal damping as the multiplication of $\hat{c}$ with $\hat{m}$. Using this, the MTF can be mathematically described by the absolute value of the Fourier transform of the convolution kernel $\hat{m}$, i.e.,

$$\mathrm{MTF}(\nu) := \frac{|\hat{m}(\nu)|}{|\hat{m}(0)|}. \tag{2.115}$$

Usually, the MTF is normalized in such a way that structures of spatial frequency $\nu = 0$ have unit contrast. In Fig. 2.37, the MTF of the MPI imaging kernel is plotted for different particle diameters and a particle size distribution. While the shape of the MTF on a logarithmic scale is concave for monosized particles, it is convex for polysized particles. For each spatial frequency, one can find a corresponding particle diameter, for which the MTFs for mono- and polysized particles have the same decay. The MTF of polysized particles is, however, orders of magnitudes lower

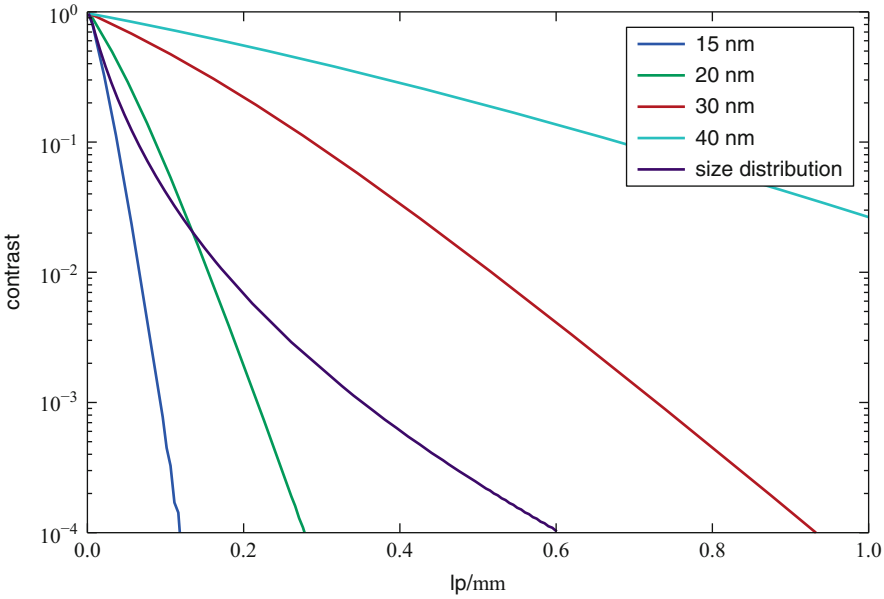

Fig. 2.37 MTF of the MPI process for different particle diameters and a particle size distribution (log-normal distribution with mean value 16.4 nm and standard deviation 4 nm)

such that the contrast that is required to resolve the same structure is significantly higher for polysized particles. This indicates that MPI would greatly benefit from particles having a very narrow size distribution that potentially increases the SNR and in turn the sensitivity of the method.

Usually, the MTF is plotted versus line-pairs (lp) per millimeter. To obtain a length of two objects to be separated by a certain contrast variation, one might consider the reciprocal of the spatial frequency. However, $\frac{1}{\nu}$ would be the length of a line pair that is resolved. To convert the spatial frequency into a length R, which gives the width of the smallest line that can be resolved, one should therefore use $R = \frac{1}{2\nu}$.

The loss in contrast described by the MTF can be compensated by performing a reconstruction. To discuss the maximum resolution of the imaging system for a certain MTF and SNR, in the following a sinusoidal particle concentration

$$c(x) = c_0(1 + \sin(2\pi\nu_0 x)) \tag{2.116}$$

is considered as the object. The spectrum of $c(x)$ has three delta peaks at frequencies $-\nu_0$, 0 and ν_0. For a constant noise level σ, the SNR at frequency ν_0 can be computed by

$$\mathrm{SNR}(\nu_0) = \frac{c_0|\hat{m}(\nu_0)|}{\sigma} = \frac{c_0\mathrm{MTF}(\nu_0)|\hat{m}(0)|}{\sigma}. \tag{2.117}$$

As the MTF of the MPI process is monotonically decreasing for increasing frequency (see Fig. 2.37), the SNR decreases for increasing frequency as well. Hence, one can find for a certain SNR a corresponding frequency ν_0. If the SNR drops below 1, the signal cannot be recovered. Hence, to compute the maximum frequency $\nu^{\max}$, one can insert $\mathrm{SNR}(\nu^{\max}) = 1$ and solve for the frequency $\nu^{\max}$ yielding

$$\nu^{\max} = \mathrm{MTF}^{-1}\left(\frac{\sigma}{c_0|\hat{m}(0)|}\right). \tag{2.118}$$

Note, that MTF^{-1} is the inverse of the MTF, which gives the resolution for a certain contrast. It should not be mixed up with the inverse of the Fourier transformation $\mathcal{F}^{-1}$. The argument in (2.118) is actually the inverse of the SNR for frequency zero, i.e., for constant signal. Thus, the maximum frequency that can be resolved is given by

$$\nu^{\max} = \mathrm{MTF}^{-1}\left(\frac{1}{\mathrm{SNR}(0)}\right). \tag{2.119}$$

By taking the half of the reciprocal of the spatial frequency, the maximum resolution can be expressed as

$$R^{\mathrm{MTF}} = \frac{1}{2\nu^{\max}} = \frac{1}{2\mathrm{MTF}^{-1}\left(\frac{1}{\mathrm{SNR}(0)}\right)}. \tag{2.120}$$

For a graphical representation of this resolution expression, one can draw a horizontal line at the contrast level $\frac{1}{\mathrm{SNR}(0)}$ in the MTF plot (Fig. 2.37) and look for the intersection point with the MTF. The resulting spatial frequency on the x-axis represents the maximum that can be resolved for the given noise level.

Monosized Particles

To derive an explicit expression for the maximum resolution, we focus on monosized particles next. Unfortunately, no analytic expression for the Fourier transform of the Langevin function and in turn the MTF of the MPI process is known. To arrive at an analytical expression, one can approximate the derivative of the Langevin function by the Lorentzian

$$\zeta(\xi) = \frac{2}{\pi}\frac{2}{4+\xi^2}, \tag{2.121}$$

for which the Fourier transform is well known to be

$$\hat{\zeta}(\nu) = 2\exp\left(-4\pi|\nu|\right). \tag{2.122}$$

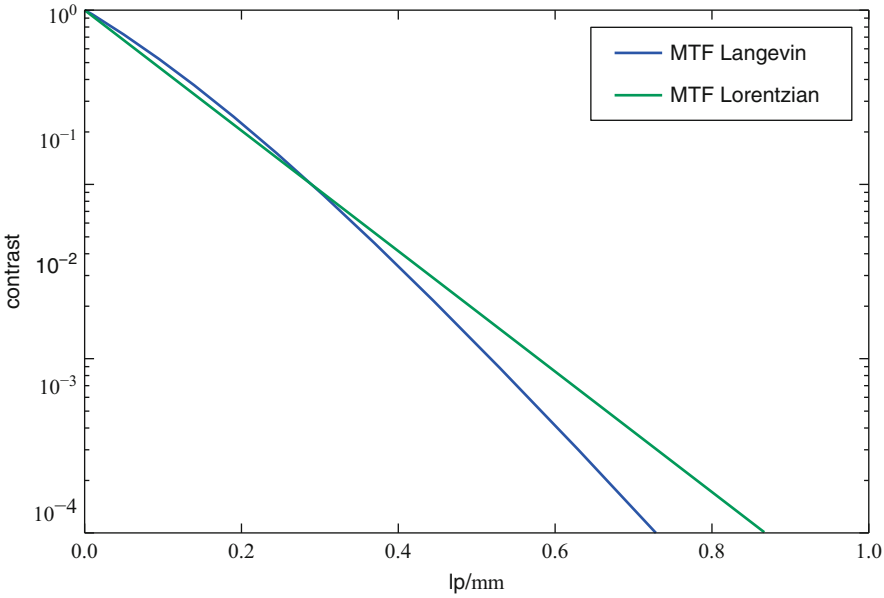

Fig. 2.38 Comparison of the numerically computed MTF of the Langevin magnetization and the MTF of the corresponding Lorentzian for Langevin particles of 30 nm diameter and unit gradient strength

Using the approximation $\mathcal{L}'(\xi) \approx \zeta(\xi)$, the MTF of the imaging process can be written in the form

$$\mathrm{MTF}(\nu, D) \approx \exp\left(-4\pi \frac{\nu}{\beta G}\right). \tag{2.123}$$

In Fig. 2.38, the numerically computed MTF of the Langevin magnetization and the corresponding MTF of the Lorentzian for 30 nm particle diameter and unit gradient strength are shown. As can be seen, the MTF of the Langevin magnetization decays slightly faster. The Fourier transform of the Lorentzian decays strictly exponentially such that the graph in the logarithmic plot shows a straight line.

The inverse of (2.123) is given by

$$\mathrm{MTF}^{-1}(C, D) \approx -\frac{\beta G}{4\pi} \ln(C), \tag{2.124}$$

where C denotes the contrast. Inserting (2.124) in (2.120) yields

$$R^{\mathrm{MTF}} \approx \frac{2\pi}{-\ln\left(\frac{1}{\mathrm{SNR}(0)}\right)\beta G} = \frac{2\pi}{\ln\left(\mathrm{SNR}(0)\right)\beta G}. \tag{2.125}$$

Comparing this resolution with that derived by the FWHM of the convolution kernel, one can see that both expressions depend on the reciprocal of β and G. However, the expression (2.125) additionally takes into account the SNR of the signal. For an SNR of about 4.6 the MTF resolution gives the same value as the FWHM resolution. An SNR of 4.6 indeed seems to be a reasonable value, for which one can identify a structure, but one is not able to increase its resolution using a deconvolution technique.

Polysized Particles

For polysized particles, the dependency of the spatial resolution on the SNR cannot be written in a simple form like (2.125). The Fourier transform of the convolution kernel for polysized particles can be written as

$$\hat{m}(\nu) = \int_0^\infty \rho(D)\hat{m}(\nu, D)\,\mathrm{d}D. \tag{2.126}$$

Hence, the MTF can be formulated as

$$\mathrm{MTF}(\nu) = \frac{\int_0^\infty \rho(D)\mathrm{MTF}(\nu, D)\hat{m}(0, D)\,\mathrm{d}D}{\int_0^\infty \rho(D)\hat{m}(0, D)\,\mathrm{d}D}, \tag{2.127}$$

i.e., the MTF of polysized particles is the superposition of the MTFs of monosized particles weighted with the probability density function $\rho(D)$. The superposition of several MTFs of monosized particles justifies the concave shape of the MTF of polysized particles illustrated in Fig. 2.37.

2.7.2 Sensitivity and Temporal Resolution

Besides the spatial resolution, the sensitivity is an essential parameter of an imaging method. Basically, the sensitivity describes the minimal amount of magnetic material that can be detected using MPI. As it has been derived in Sect. 2.7.1, the sensitivity does also influence the spatial resolution in a logarithmic fashion.

In [WBG07], the sensitivity of MPI has been investigated and the scaling law

$$\mathrm{SNR} \propto \sqrt{T^{\mathrm{meas}}} c_0 G^{-3} \frac{p^{\mathrm{R}} f^{\mathrm{E}}}{\sqrt{R^{\mathrm{P}}}} \tag{2.128}$$

has been derived. Here, T^{meas} denotes the total measurement time , c_0 denotes the mean particle concentration within a considered voxel, p^{R} is the sensitivity of the receive coil, f^{E} is the excitation frequency and R^{P} is the noise resistance of the receive coil.

In the ideal case, the noise present in the receive coil does not stem from the instrumentation itself but from eddy currents induced by the patient. As it has been shown in [Rös87], the equivalent noise resistance of a patient increases quadratically with the excitation frequency. Consequently, considering patient noise, the sensitivity of MPI is independent of the excitation frequency as the frequency and the noise resistance cancel out each other in (2.128).

Obviously, the particle concentration influences the SNR of the measured signal in a linear fashion. Furthermore, the sensitivity of the receive coil should be as high as possible to improve the SNR. In the scaling law (2.128), the sensitivity depends on the third power of the reciprocal of the gradient strength. This is based on the assumption that a change of the gradient strength is attended by a change of the voxel size that can be resolved. As MPI using the FFP encoding scheme basically measures a single voxel at a time point, the sensitivity decreases for increasing gradient strength. However, as it has been discussed in Sect. 2.7.1, the sensitivity and the spatial resolution are linked to each other such that an increase of the gradient strength does not necessarily improve the spatial resolution if the SNR of the measured signal becomes too small.

By repeating the MPI experiment several times and averaging the signals, the SNR can be improved in a square root sense. Alternatively, as it has been discussed in [KBS+09], one can increase the density of the FFP trajectory, which does improve the SNR in the same way but leads to a more independent information during a fixed acquisition time. However, an increase of sensitivity by averaging obviously comes for the cost of a decrease in temporal resolution. Therefore, in practice, the number of averages is limited by the frame rate required by the medical application.

2.7.3 Detection Limit

In order to determine the detection limit of MPI, the signal that is being generated by a definite test sample of magnetic material has to be compared to a noise signal. The lowest possible noise level is the patient noise. To determine the signal and the noise, a square-shaped single loop coil of 10 cm edge length is considered. Placing such a coil on the chest of an adult human yields an increase of the resistance of the coil of approximately $100\,\mathrm{mT}\mu_0^{-1}$ at 20 MHz, equating to a noise voltage of $R^{\mathrm{P}} = 40\,\mathrm{pV}/\sqrt{\mathrm{Hz}}$ root-mean-square, calculated from

$$u^{\mathrm{noise}} = \sqrt{4k_{\mathrm{B}}T^{\mathrm{P}}f^{\mathrm{S}}R^{\mathrm{P}}}, \tag{2.129}$$

where f^{S} is the frequency bandwidth (see [Joh28]). To determine the signal strength, it is assumed that in a finite volume V^{sample}, a given total magnetization oscillates with a given frequency, leading to

$$u^{\mathrm{signal}} = 2\pi p^{\mathrm{R}} f^{\mathrm{E}} M V^{\mathrm{sample}} \cos(2\pi f^{\mathrm{E}} t), \tag{2.130}$$

where f^{E} is the excitation frequency, M is the magnetization and $p^{\mathrm{R}} = 10^{-6}\,\mathrm{TA}^{-1}$ is the coil sensitivity of the test coil. The product of the magnetization M and the volume V^{sample} is a dipole moment, the value of which is $92\,\mathrm{fAm}^2$, assuming that the test sample consists of 1 pg of iron oxide available in a finite volume. Using (2.130), this results in a signal strength of 12 pV peak and about 8 pV root-mean-square. To ensure the detectability of the signal, the arbitrary choice is made, that the signal strength has to be five times higher than the noise, which would be 200 pV. This corresponds to 25 pg of iron in a given, finite volume. This derivation assumes a frequency bandwidth of 1 Hz, which corresponds to a measurement time of 1 s. Prolonging the measurement to, e.g., 625 s – a little more than 10 min – leads to a frequency bandwidth of 1/625 and, following (2.129), to a decrease in the noise by a factor of 25. This, in turn, would also lower the demand on the signal by a factor of 25 and thus lower the detection limit to 1 pg iron oxide.

To convert these amounts of material into concentrations, usually expressed by the number of iron atoms per liter of solvent/dispersion, the magnetic material contained in one voxel has to be considered. As the molar mass of iron oxide (Fe_3O_4) is $231.5\,\mathrm{g\,mol}^{-1}$, 1 g of iron oxide contains about 4.32 mmol iron oxide and thus about 13 mmol iron and, therefore, 1 pg of iron oxide contains about 13 fmol iron. Assuming that this number of iron atoms is contained in a voxel of $1\,\mathrm{mm}^3$, the concentration in this voxel will be about $13\,\mathrm{fmol(Fe)mm}^{-3}$, corresponding to a detectable concentration of about $13\,\mathrm{nmol(Fe)l}^{-1}$.

Starting from 25 pg instead of 1 pg, implying a measurement time of 1 s instead of about 10 min, yields a detection limit of $324\,\mathrm{nmol(Fe)l}^{-1}$ for a voxel size of $1\,\mathrm{mm}^3$. Resovist® has an undiluted concentration of $500\,\mathrm{mmol(Fe)l}^{-1}$. Applied according to prescription, 1.4 ml of undiluted Resovist® is administered for one examination during an MRI scan. Assuming an adult human's blood volume to be 6 l, this results in a steady state concentration of $116\,\mathrm{mol(Fe)l}^{-1}$, about 360 times the detection limit for a voxel size of $1\,\mathrm{mm}^3$ and a measurement time of 1 s.

All these estimations imply that MPI is being used as a single voxel method, i.e., the concentration of the magnetic material is measured one voxel at a time. Using more effective coding schemes, as exemplified in Sect. 6.3, can increase the detection limit by about one order of magnitude.

http://www.springer.com/978-3-642-04198-3

Magnetic Particle Imaging
An Introduction to Imaging Principles and Scanner Instrumentation
Knopp, T.; Buzug, T.M.
2012, X, 204 p., Hardcover
ISBN: 978-3-642-04198-3